Economic model predictive control for packed bed chemical looping combustion

Gabriel D. Patrón[a], Kayden Toffolo[a], Luis Ricardez-Sandoval[a]*

[a]Department of Chemical Engineering, University of Waterloo, Waterloo, ON, Canada N2L 3G1

Abstract

This study presents an economic model predictive control (EMPC) scheme for the packed-bed reactor (PBR) design of a chemical looping combustion (CLC) system. This scheme is enabled by a pseudo-homogeneous process model, which accurately represents the macroscopic process behaviour, and enables economics to be optimized online. Both CLC stages are optimized whereby the oxidation stage considers energy generation and inert gas use, while the reduction stage economizes CO_2 production and fuel use. To understand the behaviour of the EMPC, the scheme is tested on a CLC plant represented by a multi-scale process model. Both stages are tested under varying initial inlets, energy prices, carbon prices, and fuel prices. The optimal policy for the oxidation stage is found to be that of maximal peak temperature, where the EMPC results in revenue while the previous state-of-the-art controller results in losses. The optimal reduction stage behaviour is highly dependent on carbon and fuel prices whereby a trade-off between CO_2 selectivity and throughput are observed. An EMPC approach is found to be economically superior to advanced regulatory control with up to an order-of-magnitude and ~33% improvements in the oxidation and reduction stages, respectively. This study represents a step forward towards the adoption of the intensified PBR CLC process as an emerging and viable technology for heat generation with inherent CO_2 capture.

Keywords: Chemical looping combustion; economic model predictive control; closed-loop control; carbon capture

*Corresponding author: e-mail: laricard@uwaterloo.ca, phone: (+1) 519 888 4567 x38667, fax, (+1) 519 888 4347

1. Introduction

Despite the continued deployment of renewable energy technologies, fossil fuels remain embedded in the global energy system, accounting for ~80% of worldwide energy mix [1]. Natural gas, mainly comprised of methane, emits less carbon than other fossil fuels and accounts for about quarter of global electricity production [1]. Accordingly, it has been touted as a transitional fuel while full renewable deployment occurs [1, 2]. Although cleaner than coal and petroleum, CO_2 is nonetheless produced in methane combustion, thus carbon capture and storage (CCS) has been proposed as a strategy to abate the emissions created by natural gas. However, the cost of carbon capture remains high [3] primarily owing to the separation of CO_2 from the flue gas [4].

Chemical looping combustion (CLC) has been proposed as a potential avenue for reducing the separation burden in CCS, which has inhibited its development owing to high costs [5]. CLC employs "inherent" carbon capture as its flue gas contains components that are inexpensively separated (e.g., steam) unlike conventional combustion methods. A CLC reactor is an intensified process that operates by cycling between oxidation and reduction stages. The oxidization stage feeds air and inert gas to provide oxygen to a metallic oxygen carrier (OC), whereby an exothermic reaction occurs, and the heated air mixture can be routed to a turbine for energy generation. The reduction stage subsequently regenerates the OC using a gaseous or gasified fuel (e.g., natural gas or syngas), which undergoes combustion to generate CO_2 and water. As the water is easily condensed from the reduction products, there is little flue gas separation burden and near complete capture can be achieved [5] in comparison to conventional CCS, which can achieve ~95% capture in the best of cases and at high costs [4]. CLC was originally designed as two interconnected fluidized bed reactors wherein the OC was cycled between the air and fuel reactors. More recently, CLC in a packed bed reactor (PBR) has been proposed [6] to avoid the cyclone necessary to separate the OC and the hot gas; this also increases combustion efficiency and features a more compact reactor, thus intensifying the traditional CLC process.

CLC systems are typically operated with constant inlet flowrates of air/inert and fuel in the oxidation and reduction stages, respectively [6, 7, 8]. Increasingly, the control of CLC systems is being investigated to improve energy output and utility use. To this regard, Gu et al. [9], Kim et al. [10], Wang et al. [11], and Wanotayaroj et al. [12] have deployed conventional feedback (PID) controllers in CLC systems to regulate reactor temperatures using heaters. Moreover, model-based dynamic optimization and optimal control have also been applied to CLC by Lucio & Ricardez-Sandoval [13], Parker & Biegler [14], and Toffolo & Ricardez-Sandoval [15]; these scheme aim to deploy time-varying inlet flowrates to regulate outlet temperature, conversion, pressure, and component concentrations. Notably, while the aforementioned schemes aim to regulate towards pre-specified set points, Han & Bollas [16] deployed a dynamic optimization scheme that maximizes outlet temperature over a CLC PBR cycle, thus explicitly optimizing for a performance metric.

Another important factor in the operation of CLC, and indeed all PCC processes, is the cost. For CLC, some work has been conducted in techno-economic optimization, which optimizes design parameters and operating conditions subject to long-term costs. For instance, Iloeje et al. [17] optimized the levelized cost of electricity as well as process efficiency of a rotary-bed CLC. More recently, Okoli et al. [18] optimized the total annualized process cost, which consisted of equipment and operating costs for a moving bed CLC. Both technoeconomic studies considered the reactor geometries as decision variables, while the latter also considered inlet conditions (e.g., flowrates and pressures). While these

previous optimization studies make offline (i.e., not implemented in the plant real-time) decisions, the economic considerations explored therein (e.g., operating costs) can be adapted for online decision making. Economic objective functions optimized online could provide an avenue for improvement in process cost through smarter real-time allocation of utilities subject to market conditions and upstream disturbances.

The optimization and advanced model-based control of CLC necessitate the application of comprehensive dynamic process models that capture the behaviour of the process with sufficient detail. To this end, several mechanistic and reduced order CLC models have been proposed in the literature. Noorman et al. [6] first proposed a homogeneous (i.e., macroscale) and then a multi-scale model [19, 20] for the dynamics of a PBR CLC with a copper-based OC. Subsequently, Han et al. [7, 21] also proposed a multi-scale model for a PBR CLC with a nickel-based OC.

For dynamic processes like CLC, economic model predictive control (EMPC) [22] can provide a way to reconcile the economic optimization and process control problems. EMPC solves a dynamic optimization problem to determine the economically optimal inputs while considering constraints, which ensure realistic and safe operational limits are observed. Moreover, it can accommodate for changing market conditions (e.g., prices) by adjusting the operating policy to meet changing incentives. In the PBR case, the operation of each CLC stage is on the timescale of hours; this necessitates requires a short-term online optimization paradigm such as EMPC, which uses an internal process model to predict the process economics into the future and can be re-solved at a high frequency. By determining economically optimal control actions, EMPC can serve to intensify processes by enabling the economical dynamic generation of products and allocation of utilities; this can further improve the performance of an already intensified dynamic process like PBR CLC.

Several studies have identified process intensification as an avenue to achieve sustainability, cost reduction, and energy efficiency goals [23–25]. The benefits from an intensified process like PBR CLC can be further augmented through control and economic optimization [24, 25]. Based on the review above, there is a gap pertaining to the economically optimal dynamic operation of CLC systems. To the authors' knowledge, no previous studies have considered the use of EMPC for CLC, likely owed to the difficulty in implementing a detailed process model that facilitates optimizing the process economics online. No economic functions for online deployment have been proposed for the CLC stages; to this end, we propose novel economic functions for both reduction and oxidation stages, which jointly maximize production while minimizing utility expenditure. The economic optimization problem is enabled by a pseudo-homogeneous process model that accurately predicts macroscopic system dynamics while remaining computationally parsimonious; the decisions of this model are tested in a simulated plant represented by a highly detailed multi-scale industrial process model.

This study is organized as follows: section 2 provides general formulations for the economically optimal predictive control of CLC; section 3 presents a case study of nickel-based OC PBR described by both pseudo-homogenous and a multi-scale models; section 4 tests the proposed scheme in both CLC stages; section 5 provides conclusions and future work directions.

2. Proposed CLC EMPC formulations

The CLC stages are semi-batch (i.e., stage-wise) processes whereby products are generated while continually expending utilities. In the reduction stage, the product is energy while the utility is the inert gas. In the oxidation stage,

a high-purity CO_2 product is generated while expending fuel. Traditionally, CLC has used constant (i.e., time-invariant) feed flowrates; the control approaches reviewed in the previous section take the first steps in removing this assumption. Herein, we also propose the dynamic use of feed streams; however, we advance the existing CLC control literature by deploying an EMPC as depicted in Figure 1.

The main principle behind EMPC is to solve a dynamic optimization problem with an economic objective function; this allows for the optimal allocation of the input trajectory such that the income-generating product of a process is maximized while utilities are minimized. The solution to the EMPC problem is recurrently deployed online (i.e., in the plant) and feedback is provided such that the input decisions can be updated subject to the current plant state. In the context of CLC, EMPC can further intensify the process by optimally allocating the air/inert feeds to maximize energy generation in the oxidation stage and the fuel feed to maximize CO_2 avoidance in the reduction stage. The EMPC-specified actuation of these feeds is favourable to tracking control (e.g., MPC), which regulates the system towards pre-specified set points that may not be economically optimal. Further, EMPC is well suited to CLC as it can adjust its operating policy to changing economic conditions; since the CLC stages are usually short, these changes will typically occur between (and not within) stages.

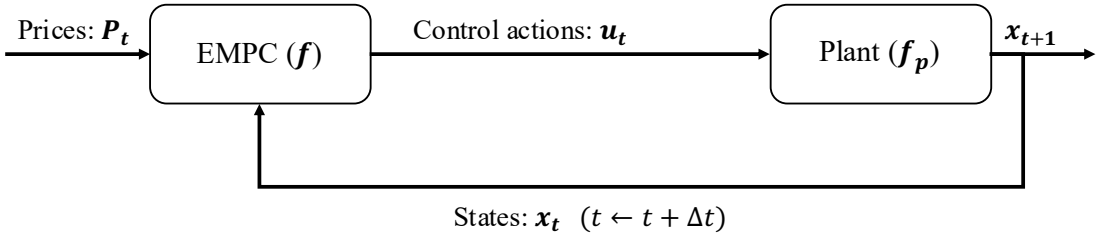

Figure 1: Proposed EMPC scheme.

As shown in Figure 1, an EMPC works to provide economically optimal control actions to the plant subject to changing economic incentives. The plant is operated for a given time interval (Δt), upon which the states are provided as feedback to the EMPC, which makes the scheme closed-loop. An EMPC formulation, stated generally as to apply to any CLC configuration, is as follows:

$$
\begin{aligned}
&\max_{\boldsymbol{u_{t+j}}} \sum_{j=1}^{P} \phi_\pi(\boldsymbol{P_t}, \hat{\boldsymbol{x}}_{\boldsymbol{t+j}}) - \phi_v(\boldsymbol{P_t}, \boldsymbol{u_{t+j}}) \\
&\boldsymbol{f}\left(\hat{\boldsymbol{x}}_{\boldsymbol{t+j}}, \boldsymbol{u_{t+j}}\right) = \hat{\boldsymbol{x}}_{\boldsymbol{t+j+1}} && \forall j \in \{0, \dots, P-1\} \\
&\hat{\boldsymbol{x}}_{\boldsymbol{t}} = \boldsymbol{x_{fdbk}} && (1) \\
&\boldsymbol{g}\left(\hat{\boldsymbol{x}}_{\boldsymbol{t+j}}, \boldsymbol{u_{t+j}}\right) \leq \boldsymbol{0} && \forall j \in \{1, \dots, P\} \\
&\boldsymbol{u_{t+j}} \in \boldsymbol{\mathcal{U}} && \forall j \in \{1, \dots, P\} \\
&\boldsymbol{u_{t+j}} = \boldsymbol{u_{t+j+1}} && \forall j \in \{C, \dots, P-1\}
\end{aligned}
$$

where, respectively, $\hat{\boldsymbol{x}}_{\boldsymbol{t+j}} \in \mathbb{R}^{n_x}$ and $\boldsymbol{u_{t+j}} \in \mathbb{R}^{n_u}$ denote the predicted states and manipulated variables at time j in the future. The model $\boldsymbol{f}$: $\mathbb{R}^{n_x} \times \mathbb{R}^{n_u} \rightarrow \mathbb{R}^{n_x}$ maps the states of the systems and the inputs on the prediction horizon P such that the dynamics of the systems are predicted (Figure 2). The current (i.e., at time t when the EMPC problem is executed) states of the system are obtained as feedback from the plant ($\boldsymbol{x_{fdbk}} \in \mathbb{R}^{n_x}$) and fixed at $j = 0$ on the horizon ($\hat{\boldsymbol{x}}_{\boldsymbol{t}}$, Figure 2); by conveying feedback in this way, the predictions remain accurate. The EMPC can also address any

trajectory constraints that the process may have, where $\boldsymbol{g}: \mathbb{R}^{n_x} \times \mathbb{R}^{n_u} \rightarrow \mathbb{R}^{n_g}$ maps the states and the inputs to the constraints on the prediction horizon P such that any safety, purity, and performance goals are satisfied.

The manipulated variables on the control horizon C are the decision variables for the EMPC problem. They are bounded within the feasible region $\boldsymbol{\mathcal{U}}$, which contains realistic ranges for actuation. $C \leq P$, thus, beyond the control horizon, the manipulated variables are fixed until the end of the prediction horizon; this is done through the last constraint in (1) and shown in Figure 2.

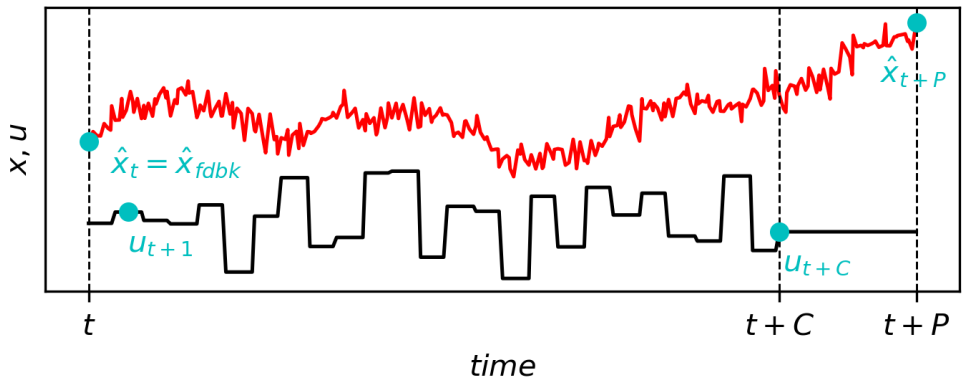

Figure 2: Key predictive control points.

The objective function is composed of product (π) and utility (υ) terms, $\phi_\pi \in \mathbb{R}$ and $\phi_\upsilon \in \mathbb{R}$, respectively. The economic objective is dependent on the unit prices ($\boldsymbol{P_t} \in \mathbb{R}^{n_P}$), which are assumed to be time-invariant (i.e., constant) in the prediction horizon P wherein the profit is maximized while utility use is minimized in the objective function. Constant prices are assumed in the present study as CLC systems operate on a short timescale wherein the relevant markets (e.g., energy) are relatively stable. However, we note that market changes can be incorporated into the EMPC economic model by indexing the pricing vector with respect to the horizon (i.e., if a pricing schedule is known) or by updating the price vector at each EMPC iteration (i.e., if price fluctuations are detected). By optimizing the trajectory of the economic quantities, the ongoing production and consumption of products and utilities in the CLC outlet and inlet are, respectively, allocated optimally. In particular, the dynamic optimization of the economic function allows for dynamically varying inputs as shown in Figure 2; this is novel within the CLC literature as discussed in section 1 and serves to minimize resource use. As mentioned in section 1, no economic functions have been proposed previously for online use in a CLC system. Herein, we propose distinct economic functions for each stage and state them generally so they can be applied in any CLC design. The optimization criteria for the oxidation stage are energy generation and inert use, while the criteria for the reduction stage are CO_2 avoided, downstream separation burden, and fuel consumption; these are presented in detail next.

2.1. Oxidation economics

The CLC uses a cold air stream to oxidize the metal OC in the reactor. In doing so, the air is heated to $T_{out}(K)$ such that it is used as the working fluid in a gas turbine. Additionally, inert N_2 gas is often used to increase the flowrate of the inlet or to dilute the oxygen concentration in the air stream, thus the total inlet to the CLC is $F_{in} = F_{air} + F_{N_2}(mol/s)$. The product ($\pi$) and utility ($\upsilon$) for this stage are the energy from the hot air and the inert inlet,

respectively. The product term in the objective function for (1) is expressed as follows for the oxidation stage at time j:

$$\phi_{\pi,ox,j} = P_e \eta F_{tot,out,j} C_{p,f} (T_{out,j} - T_{ref}) \quad (2)$$

where $F_{out,tot}(mol/s)$ denotes the total molar outlet flowrate of heated gas. $P_e(\$CAD/kWh)$ is the commercial electricity price (e.g., Ontario prices [26] to which the appropriate unit conversions must be applied); this is the price at which the energy produced by the CLC is sold to consumers. $C_{p,f}$ is the outlet fluid heat capacity [13]; the sensible heat in the CLC outlet air is assumed to carry all the energy for power generation herein (i.e., only a gas turbine is considered and not a combined cycle); however, equation (2) can be adjusted for other forms of heat transfer (e.g., latent). η is an electrical generation efficiency factor, which accounts for the downstream thermal efficiency of the turbine [27]. T_{ref} is the gas turbine outlet temperature [15], which allows for calculating the amount of sensible heat extracted from the gas.

Furthermore, the utility term for the oxidation stage can be represented at time j as follows:

$$\phi_{v,ox,j} = P_{N_2} \dot{V}_{N_2,in,j} \quad (3)$$

where $\dot{V}_{N_2,in,j}$ (m^3/s) denotes the inlet volumetric flowrate of inert gas and $P_{N_2}(\$CAD/m^3)$ is the cost of inert N_2, which is typically denominated on a volumetric basis [28].

2.2. Reduction economics

Once the CLC oxidation stage occurs, the OC must be reduced by a fuel such that it can eventually be re-used for energy generation. To do so, a gaseous (or gasified) fuel, with inlet flowrate $F_{fuel}(mol/m^2/s)$, is used for combustion on the oxidized OC. The reactor outlet in this stage is composed of the combustion products; the most expensive of these are the CO_2 and the unreacted fuel. Accordingly, the product (π) and utility (v) for this stage are the CO_2 and the fuel inlet, respectively. The product term in the objective function for (1) is expressed as follows for the reduction stage at time j:

$$\phi_{\pi,red,j} = P_{CO_2} \dot{m}_{CO_2,out,j} \quad (4)$$

where $\dot{m}_{CO_2,out,j}(tn/s)$ denotes the mass flowrate of carbon dioxide produced in the CLC and $P_{CO_2}(\$CAD/tn)$ is the carbon price, which is typically denoted on a tonne basis [29]. This term is maximized as nearly all CLC-produced CO_2 can be utilized or stored. Thus, equation (4) effectively represents an avoided carbon tax that would have been paid if CO_2 was released into the environment by an emissive combustion method; the inherent carbon capture in CLC avoids these emissions. Moreover, the utility term for the reduction stage is as follows at time j:

$$\phi_{v,red,j} = P_{fuel} \dot{V}_{fuel,in,j} + P_{sep} \dot{V}_{fuel,out} \quad (5)$$

where $\dot{V}_{fuel,in,j}$ and $\dot{V}_{fuel,out}(m^3/s)$ denote, respectively, the inlet and outlet volumetric flowrates of fuel (the latter represents the unreacted fuel). Moreover, $P_{fuel}(\$CAD/m^3)$ and $P_{sep}(\$CAD/m^3)$ are, respectively, the fuel price [30]

and downstream separation price [31]. The former cost terms disincentivizes the consumption of fuel while the latter term can increase CO_2 purity in the outlet stream such that the amount of unused fuel is minimized, thus also minimizing any further downstream separation burden.

3. PBR CLC models

With respect to traditional energy generation methods CLC, is intensified as it has inherent carbon capture, whereby the flue gas will contain high CO_2 purity and condensable species, avoiding the need for the costly downstream separation in conventional CCS. The process models in the present study are based on Toffolo et al. [32], which used a nickel-based OC for an industrial-scale CLC PBR. The PBR layout further employs intensification as both stages are carried out in a single vessel, thus avoiding an OC separation unit, and making the process more modular. As outlined previously, the CLC system contains interacting multi-scale phenomena and operates in oxidation and reduction stages; these are depicted in Figure 3. A column layout with inlets at the bottom (0) and outlets at the top (L) is adopted with a cross-sectional area $A_z(m^2)$; the streams in this column design are denominated as fluxes (G). As with Toffolo et al. [32], methane (CH_4) is used as fuel in the present study.

As per this coordinate system, the outlet temperature and CO_2 flow variables defined in section 2.1. and section 2.2., respectively, can be specified as $T_{out} = T_{z=L}(K)$ and $\dot{m}_{CO_2,out}(tn/s) = G_{CO_2,z=L}A_z M_{CO_2}$ where $M_{CO_2}(tn/mol)$ denotes the molar mass of CO_2. Further, the inlets for the oxidation stage are $\dot{V}_{N_2,in,j}\ (m^3/s) = G_{N_2}A_z V_{m,N_2}$ and $\dot{V}_{air,in,j}\ (m^3/s) = G_{air}A_z V_{m,air}$ while the inlet for the reduction stage is $\dot{V}_{fuel,in} = G_{CH_4}A_z V_{m,CH_4}$ where $V_{m,i}$ denotes molar volumes. These inlets and outlets are shown in Figure 3.

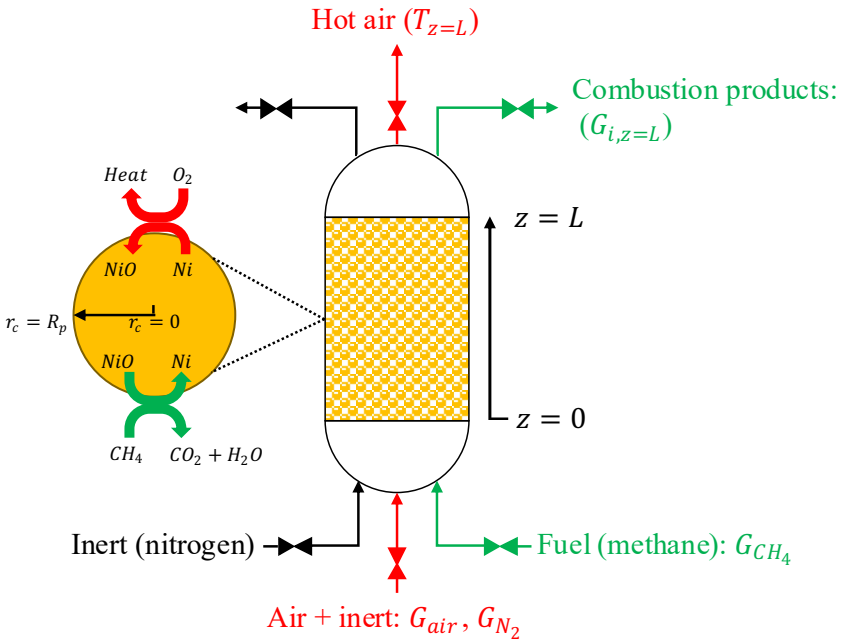

Figure 3: CLC PBR axial and particle radial domains; red depicts oxidation stage and green depicts reduction stage.

The length of the packed bed is denoted by the variable $z \in \{0, \dots, L\}$ and the particle radii are denoted by the variable $r_c \in \{0, \dots, R_p\}$; these are the spatial coordinates that the CLC system is distributed in. Moreover, CLC is a dynamical

process, thus it is also variable with respect to the temporal domain t. The reduction stage contains the components $i = \{CH_4, H_2, CO, CO_2, H_2O, N_2\}$, while the oxidation stage contains $i = \{O_2, N_2\}$. Danckwerts boundary conditions are used for this system; these are common for PBRs [33] since they impose gradients corresponding to multi-phase and bulk-boundary mass/energy transfer. The column design parameters and nominal operating conditions for the CLC system are listed in Table 1. No intra-stage disturbances were considered in the present study as the focus was on pricing; however, stochastic disturbances in inlet feed properties (e.g., temperature, Table 1) could affect the EMPC operation of the CLC PBR.

Table 1: Nickel OC PBR design parameters and nominal operating conditions.

Design parameter	**Symbol (units)**	**Values**
Reactor length [32]	$L(m)$	11
Reactor diameter [32]	$D(m)$	5.5
Particle diameter [32]	$D_c(mm)$	5
Particle porosity [32]	ε_c	0.4
Operating condition		
Initial nickel concentration [32]	$C'_{Ni,0}(kg/kg\ OC)$	0.3
Inlet temperature [32]	T_{in}(℃)	450
Inlet pressure [32]	$P_{in}(bar)$	17
Gas turbine outlet temperature [15]	$T_{ref}\ (K)$	723
Efficiency factor [27]	η	0.41

As mentioned previously, both multi-scale and pseudo-homogeneous models are deployed this study and follow the conditions specified in Table 1. While the multi-scale model provides excellent prediction accuracy in both particle and packed bed axial quantities, modelling two spatial domains evolving at different timescales is computationally expensive and difficult to solve with conventional optimization solvers. Instead, the pseudo-homogeneous model, which assumes a homogeneous particle domain while yielding good macroscopic process predictions, is deployed for the EMPC as it has reduced model complexity and lower computational cost. Both models use Danckwerts boundary conditions, contain the same chemical components, use the same reaction kinetics, and model the axial domain. The main difference occurs in the pseudo-homogeneous model, which does not consider the radial domain of the particle, thus not fully capturing the particle-bulk interactions.

The model developed and validated in Toffolo et al. [32] was found to be in good agreement with the experimental data from Hamers et al. [8] and Han et al. [16] for the oxidation stage as well as the data from Jin and Ishida [34] and Spallina et al. [35] for the reduction stage. The differential conservation equations in both models are outlined next, the reader is referred to Toffolo et al. [32] for details on algebraic equations.

3.1. Multi-scale (MS) model

The multi-scale model makes the following assumptions:

1. The feed is uniformly distributed in the reactor radius.
2. The gas velocity is constant in the spatial domains.

3. The OC particles are perfectly spherical with uniform distribution of nickel on their surface.
4. The OC particles are uniformly distributed within the PBR.
5. The macroscopic structure of the OC is uniform and not affected by the reactions.
6. The gas within the OC radial domain is the same temperature as the particle.
7. The thermal conductivity of the gas is negligible with respect to that of the OC.
8. There is negligible heat loss to the environment.

In the present study, the multi-scale model is deployed as the simulated plant model, i.e. it represents the plant in our computational framework shown in Figure 1.

3.1.1. Multi-scale material balances

The material quantities in the reactor are modelled to determine combustion efficiency, conversion, and recovery rates. As the bulk fluid reacts with the OC, thus depleting or enriching the OC, material balances for both are carried out. As shown in equations (6)–(11), the macro and micro-scale models both consider component diffusivities; however, the reactions are assumed to occur in the micro-scale while the throughput (i.e., flowrates) are modelled in the macro-scale. The bulk reaction material balance, along with its corresponding boundary conditions, are as follows:

$$\varepsilon_b \frac{\partial C_i}{\partial t} + \frac{\partial F_i}{\partial V} = \frac{\partial}{\partial z}\left(D_{ax,i} \frac{\partial C_i}{\partial z}\right) + k_{c,i} a_v \left(C_{c,i|r_c=R_p} - C_i\right) \tag{6}$$

$$\varepsilon_b D_{ax,i} \frac{\partial C_i}{\partial z}\bigg|_{z=0} = \frac{F_i|_{z=0} - y_{i,in} F_{in}}{A_z} \tag{7}$$

$$\frac{\partial C_i}{\partial z}\bigg|_{z=L} = 0 \tag{8}$$

where $C_i(mol/m^3)$, $F_i(mol/s)$, $k_{c,i}(m/s)$, $D_{ax,i}(m^2/s)$, $C_{c,i|r_c=R_p}(mol/m^3)$, and $y_{i,in}(mol/mol)$ denote, respectively, the component bulk concentrations, flowrates, rate constants, diffusivities, particle-bulk boundary concentrations, and inlet molar fractions. F_{in} denotes the total inlet flowrate to the reactor, while ε_b and $a_v(m^2/m^3)$ are, respectively, the bed porosity and the volume-specific particle surface area. The particle material balance, and its associated boundary conditions, are as follows:

$$\varepsilon_c \frac{\partial C_{c,i}}{\partial t} = \frac{1}{{r_c}^2} \frac{\partial}{\partial r_c}\left(D_{e,i} {r_c}^2 \frac{\partial C_{c,i}}{\partial r_c}\right) + \varepsilon_c \rho_s \sum_{j=1}^{n_r} r_{i,j} \tag{9}$$

$$-D_{e,i} \frac{\partial C_{c,i}}{\partial r_c}\bigg|_{r_c=R_p} = k_{c,i}\left(C_{c,i}|_{r_c=R_p} - C_i\right) \tag{10}$$

$$\frac{\partial C_{c,i}}{\partial r_c}\bigg|_{r_c=0} = 0 \tag{11}$$

where $C_{c,i}(mol/m^3)$ and $D_{e,i}(m^2/s)$ denote the component particle concentrations and diffusivities. $r_{i,j}(mol/kg/s)$ denote the component reaction rates in the j^{th} reaction. $\rho_s(kg/m^3)$ is the solid density while ε_c is the carrier porosity.

3.1.2. Multi-scale energy balances

The energy in the reactor is modelled to determine the heat generated by the reactions that can then be used for power generation. As with the material balances, the bulk and particle are constantly exchanging energy, thus balances for both are necessary. Thermal conductivity is modelled on both scales while throughput and reactivity are featured in the macro and micro-scales, respectively. The energy balance for the bulk phase, and its associated boundary conditions, are as follows:

$$\varepsilon_b C_{p,f} C_T \frac{\partial T}{\partial t} + C_{p,f} F_T \frac{\partial T}{\partial V} = \frac{\partial}{\partial z}\left(\lambda_{ax} \frac{\partial T}{\partial z}\right) + h_f a_v \left(T_{c|r_c=R_p} - T\right) \tag{12}$$

$$\varepsilon_b \lambda_{ax} \left.\frac{\partial T}{\partial z}\right|_{z=0} = \frac{C_{p,f} F_T (T_c|_{z=0} - T_{in})}{A_c} \tag{13}$$

$$\left.\frac{\partial T}{\partial z}\right|_{z=L} = 0 \tag{14}$$

where $C_T(mol/m^3)$, $T(K)$, $F_T(mol/s)$, and $T_{c|r_c=R_p}(K)$ denote the total material concentration, bulk temperature, total bulk flowrate, and particle-bulk boundary temperature. $C_{p,f}(J/mol/K)$, $\lambda_{ax}(W/m/K)$, $h_f(W/m^3/K)$ are the bulk fluid heat capacity, the bulk thermal conductivity, and the bulk-particle heat transfer coefficient. The particle energy balance, and its associated boundary conditions, are as follows:

$$\left((1-\varepsilon_c)\rho_s C_{p,s} + \varepsilon_c C_{p,c} C_T\right)\frac{\partial T_c}{\partial t} = \frac{\lambda_c}{{r_c}^2}\frac{\partial}{\partial r_c}\left({r_c}^2 \frac{\partial T_c}{\partial r_c}\right) + \varepsilon_c \rho_s \sum_{j=1}^{n_r} (-\Delta H_j) r_j \tag{15}$$

$$-\lambda_c \left.\frac{\partial T_{c,i}}{\partial r_c}\right|_{r_c=R_p} = h_f \left(T_c|_{r_c=R_p} - T\right) \tag{16}$$

$$\left.\frac{\partial T_c}{\partial r_c}\right|_{r_c=0} = 0 \tag{17}$$

where $T_c(K)$ denotes the particle temperature. $r_j(mol/kg/s)$ and $(-\Delta H_j)(J/mol)$ denote, respectively, the total reaction rate and enthalpy of the j^{th} reaction. $C_{p,s}(J/mol/K)$, $C_{p,c}(J/mol/K)$, and $\lambda_c(W/m/K)$ denote the OC heat capacity, the intra-particle fluid heat capacity, and the particle thermal conductivity, respectively.

3.2. Pseudo-homogeneous (PH) model

The pseudo-homogeneous model assumes that the intra-particle gradients are negligible such that the particles radius domain need not be modelled; this occurs when the reactions are the rate-limiting step. For accurate predictions to be yielded within this regime, the following conditions must hold:

1. $D/D_c > 100$: the particle diameters are small with respect to the reactor dimensions.
2. $h_f > 0.1\ W$: the heat transfer coefficient leads to fast macroscopic heating (i.e., not rate-limiting).
3. $k_{c,i} > 0.05\ m/s$: the mass transfer coefficients lead to fast macroscopic mass transfer (i.e., not rate-limiting).
4. $\frac{r_{i,j}\rho_s \epsilon_s {D_p}^2}{D_{e,i} C_i} < 1$: the Weisz-Prater criterion holds such that particle diffusion is not rate-limiting.

where $\epsilon_s = 1 - \epsilon_c$. These criteria were established by Han et al. [21] and Diglio et al. [36] to generate a usable range for the pseudo-homogeneous model. Toffolo et al. [32] verified that these are adhered to in the present model. The material and energy balances for the pseudo-homogeneous model are as follows:

$$\varepsilon_b \frac{\partial C_i}{\partial t} + \frac{\partial F_i}{\partial V} = \frac{\partial}{\partial z}\left(D_{ax,i} \frac{\partial C_i}{\partial z}\right) + \varepsilon_c \rho_s \sum_{j=1}^{n_r} r_{i,j} \tag{18}$$

$$\varepsilon_b C_{p,f} C_T \frac{\partial T}{\partial t} + C_{p,f} F_T \frac{\partial T}{\partial V} = \frac{\partial}{\partial z}\left(\lambda_{ax} \frac{\partial T}{\partial z}\right) + \varepsilon_c \rho_s \sum_{j=1}^{n_r} (-\Delta H_j) r_j \tag{19}$$

where all variables and parameters are defined as in the multi-scale model. As is evident from equations (18) and (19), the pseudo-homogeneous model uses the multi-scale bulk balances while incorporating the previously micro-scale reactions in its macro-scale. The resulting surrogate model is easier to simulate as less PDEs must be coupled, yet it can capture the full range of dynamics exhibited in the CLC processes. As with the multi-scale model, the Danckwerts boundary conditions corresponding to equations (7), (8), (13), and (14) are used.

3.3. Reaction kinetics

Al_2O_3-supported NiO is assumed to be the OC in this work but the EMPC scheme above is stated generally as to apply broadly. This OC was chosen by Toffolo et al. [32] as it exhibits fast kinetics, high fuel conversion, and durability. Seven reactions $n_r = 7$ with rates $r_j \forall j \in \{1, \dots, n_r\} (mol/kg/s)$ and rate constants $k_j \forall j \in \{1, \dots, n_r\} (s^{-1})$ are assumed to occur in the CLC system, which are dependent on the conversion rate of the OC, expressed as follows:

$$\frac{dX}{dt} = \frac{\sum_{j=1}^{n_r} v_j r_{Ni,j}}{C_{Ni,0}} \tag{20}$$

where X, $v_j (mol/mol)$, and $C_{Ni,0} (mol/kg\ OC)$ denote the conversion rate, stoichiometric coefficient of the j^{th} reaction, and the initial molar nickel concentration. The following reaction, with its corresponding rate, occurs in the oxidation stage:

$$2Ni + O_2 \rightarrow 2NiO: \quad r_1 = \frac{a_0 k_1}{P_{in}^{1.02}} (1 - X)^{2/3} C_{O_2} C'_{Ni,0} \tag{21}$$

where $a_0 (m^2/g\ OC)$, and $P_{in} (bar)$ denote the mass-specific surface area of OC and the inlet pressure, respectively. Concentrations denoted with an apostrophe (e.g., $C'_{Ni,0}$) are denominated in a mass basis (e.g., $kg/kg\ OC$). The oxidation rate considers assumes a shrinking core model wherein changing availability of reaction surface is accounted for; its kinetic parameters were obtained from Zhou et al. [37] and Nordness et al. [38].

The following reactions, with their corresponding rates, occur in the reduction stage:

$$CH_4 + 2NiO \rightarrow 2Ni + CO_2 + 2H_2: \quad r_2 = 2k_2 a_0 (1 - X) C_{CH_4} C_{NiO} C_{Ni} \tag{22}$$

$$CH_4 + NiO \rightarrow Ni + CO_2 + 2H_2: \quad r_3 = \frac{a_0 k_3}{P_{in}^{1.01}} (1 - X)(-\ln(1 - X))^{1 - \frac{1}{n}} C_{CH_4} C'_{NiO,0} \tag{23}$$

$$H_2 + NiO \rightarrow Ni + 2H_2O: \quad r_4 = k_4 a_0 (1 - X) C_{H_2} C_{NiO} \tag{24}$$

$$CO + NiO \rightarrow Ni + CO_2: \quad r_5 = \frac{a_0 k_5}{{P_{in}}^{1.21}} n(1-X)(-\ln(1-X))^{1-\frac{1}{n}} C_{CO} C'_{NiO,0} \tag{25}$$

$$CH_4 + H_2O \rightarrow 3H_2 + CO: \quad r_6 = \frac{k_6 \left(P_{CH_4} P_{H_2O} - \frac{{P_{H_2}}^3 P_{CO}}{K_6} \right)}{{P_{H_2O}}^{1.5696}} \tag{26}$$

$$CO + H_2O \rightarrow H_2 + CO_2: \quad r_7 = \frac{\frac{k_7}{P_{H_2}} \left(P_{CO} P_{H_2O} - \frac{P_{H_2} P_{CO_2}}{K_7} \right)}{\left(1 + K_{7,CO} P_{CO} + K_{7,H_2} P_{H_2} + K_{7,CH_4} P_{CH_4} + \frac{K_{7,H_2O} P_{H_2O}}{P_{H_2}} \right)^2} \tag{27}$$

where $C'_{NiO,0}(kg/kg\ OC)$ denotes the initial mass concentration of nickel oxide, n is a kinetic coefficient, $P_i(bar)$ denote component partial pressures. K_7, $K_{7,CO}$, K_{7,CH_4}, and $K_{7,H_2O}(bar^{-1})$ denote overall and specific adsorption coefficients.

Equations (22)–(25) represent the reduction reactions while equations (26) and (27) represent the equilibrium reactions present in the reduction stage. The reactions corresponding to Equations (22) and (24) have been observed to occur more quickly that those corresponding to equations (23) and (25) [34], which are more prevalent at the end of the reduction stage. Accordingly, a modified volumetric model is used to for equations (22) and (24), with parameters from Iliuta et al. [39], while the Avrami-Erofeev nucleation model was used in equations (23) and (25) with parameters from Han et al. [7, 21]. The equilibrium reactions (26) and (27) are, respectively, steam-methane reforming and water-gas shift. The equilibrium parameters are obtained from Numaguchi & Kikuchi [40] and Spallina et al. [35] for the former, along with Nordness et al. [38] for the latter.

3.4. Model deployment

The multi-scale and pseudo-homogeneous models outlined herein are used as the simulated plant ($\boldsymbol{f_p}$: equations (6)–(17)) and internal EMPC model ($\boldsymbol{f}$: equations (7), (8), (13), (14), (18), (19)), respectively. All operating conditions are stated in Table 1 or found in Toffolo et al. [32]. The pseudo-homogeneous model was used in the EMPC to reduce the computational effort; this is discussed in the results. Both models are discretized in the axial domain using six-point orthogonal collocations on four finite elements with Lagrange-Radau polynomials. Moreover, the multi-scale model is discretized using five central finite difference elements in the radial domain. Both models are discretized into $\tau = 10\ s$ finite time elements using backward finite differences; however, the sampling intervals and the prediction horizons vary as shown in Table 2. These discretization schemes were chosen such that the models could remain accurate while being parsimonious. Note that one solve of the multi-scale (MS) model constitutes one sampling interval while one solve of the pseudo-homogeneous (PH) model is the entire predictions horizon; as reflected in Table 2, the PH model can predict the entire horizon with slightly more variables than it take the MS model to predict one sampling interval. The study was performed on an Intel core i7-4770 CPU @ 3.4 GHz with 32 GB RAM; the simulated (MS) plant and optimization problems (PH) were implemented in Pyomo [41] with the IPOPT solver [42] used on the latter.

Table 2: Time discretization and number of equations for difference stages and models used herein.

Stage	Sampling interval (Δt)	Stage length (t_f)	Model	Prediction horizon (P)	Number of discretized equations per solve	Number of unknowns per solve
Oxidation	50 s	4000 s	MS	–	9688	–
			PH	500 s	12655	100
Reduction	30 s	1500 s	MS	–	19396	–
			PH	150 s	11699	15

As noted in Figure 3, the manipulated variables for the oxidation stage are the inert and air fluxes i.e., $\boldsymbol{u_{ox}} = [G_{air} \quad G_{N_2}]^T$. Further, the manipulated variable for the reduction stage is the methane flux $\boldsymbol{u_{red}} = [G_{CH_4}]$. These manipulated variables are bounded in the feasible regions $\boldsymbol{U_{ox}} \in \{G_{air}, G_{N_2} | 1 \leq G_{air} \leq 8{,}1 \leq G_{N_2} \leq 20\}$ and $\boldsymbol{U_{red}} \in \{G_{CH_4} | 0.2 \leq G_{CH_4} \leq 5\}$. In addition to the bounds, constraints are also set for the speed of changes in manipulated variables for each stage; this is done to ensure realistic control actions are determined by the controller such that they can be implemented in the plant. These constraints correspond to $\boldsymbol{g}$ in equation (1) and are as follows:

$$\left|\Delta \boldsymbol{u_{t+j,ox}}\right| \leq 3 \tag{28}$$

$$\left|\Delta \boldsymbol{u_{t+j,red}}\right| \leq 0.5 \tag{29}$$

where $\left|\Delta \boldsymbol{u_{t+j}}\right| = \left|\boldsymbol{u_{t+j}} - \boldsymbol{u_{t+j-1}}\right|$ is the change in the manipulated variable vector and the absolute value suppresses both sudden upwards and downwards changes. In addition to the potentially high computational cost of EMPC, which is resolved by using the pseudo-homogeneous model, EMPC-operated systems have been observed to exhibit oscillatory behaviour. This occurs as the system approaches a point where the economics of product generation and utility use are marginally different; the control move suppression term in equations (28) and (29) work to avoid this.

4. Results and discussion

The proposed EMPC is tested against the NMPC proposed by Toffolo et al. [32], which is the most advanced predictive CLC controller proposed to date. Both controllers start at the same initial conditions, are subject to the same prices, and use the same controller parameters (i.e., horizons, constraints). Only the objective functions differ between the proposed scheme and Toffolo et al. [32]; the reader is referred to the latter for tracking objective weights. The controllers were tested on the oxidation stage under varying initial inert flux conditions and energy prices while the reduction stage was tested under different fuel and carbon prices.

Both controllers are assessed based on their profit rates described in equations (2)–(5) under varying economic and operation conditions. The cumulative revenue or loss of a given CLC stage k is thus calculated as follows:

$$R_k = \tau \sum_{j=0}^{t_f} \phi_{\pi,k,j}^{p} - \phi_{\upsilon,k,j}^{p} \qquad \forall k \in \{ox, red\} \tag{30}$$

where the superscript p denotes the economics of the multi-scale simulated plant. Further, the overall revenue of one cycle of both CLC stages is denoted as $R_{CLC} = R_{ox} + R_{red}$.

4.1. Oxidation stage

As the oxidation stage is tasked with generating electricity, the revenue generated by the energy produced is the main variable of interest. Each CLC oxidation stage is run for $t_f = 3500\ s$ such that peak temperature can be achieved, and the ensuing cooldown is observed. The average EMPC CPU time was 9.4 s (i.e., this is the time needed to solve the EMPC at each sampling interval). Since this time is less than the sampling interval length (Table 2), the controller is fit for online use.

4.1.1. Initial inert flux

An initial inlet flux of inert and air must be specified before the EMPC is engaged since the controller requires feedback to be solved. Toffolo et al. [32] assumed initial inlets of $G_{air,0} = 1\ kg/m^2/s$ and $G_{N_2,0} = 20\ kg/m^2/s$, whereby the high initial inert rate is used to accelerate the heat front to the outlet. Herein, the economics associated with varying initial inert fluxes are studied by running the EMPC and NMPC-operated CLC systems with varying initial fluxes as summarized in Table 3. These results use the Ontario mid-peak energy price of $P_e = 0.122\ \$CAD/kWh$ [26], which is relatively low by international standards [43].

Table 3: Cumulative revenue for varying initial inert flux at Ontario mid-peak energy prices.

$\boldsymbol{G_{N_2,0}(kg/m^2/s)}$	$-$	5	10	15	20
$\boldsymbol{R_{ox}}$ ($\boldsymbol{\$CAD/stage}$)	***EMPC***	858.17	610.96	84.10	−692.51
	NMPC **[32]**	−4868.37	−6532.77	−6884.45	−6891.57

It should first be noted that the EMPC outperforms the NMPC on an economic basis for all initial inert fluxes as shown in Table 3. Moreover, for all NMPC implementations and the EMPC with high initial flux ($G_{N_2,0} = 20\ kg/m^2/s$), the revenue is negative, thus the process is operating at a loss. Figure 4 exemplifies why this loss occurs in the NMPC; in these cases, the inert inlet (Figure 4b) corresponds to initial prolonged period of negative profit (Figure 4d). Additionally, the regulatory objective of the NMPC supresses the peak temperature to $900°C$ (Figure 4c), thus not enough energy is generated to offset the cost of inert. On aggregate, the regulatory objective, while maintaining near the set point temperature for much of the stage, is economically suboptimal. From a control standpoint, the NMPC uses two coordinated pulses of inlets (Figure 4a and b) to achieve good regulation; this leads to two temperature peaks occurring before significant cooling occurs towards the end of the stage.

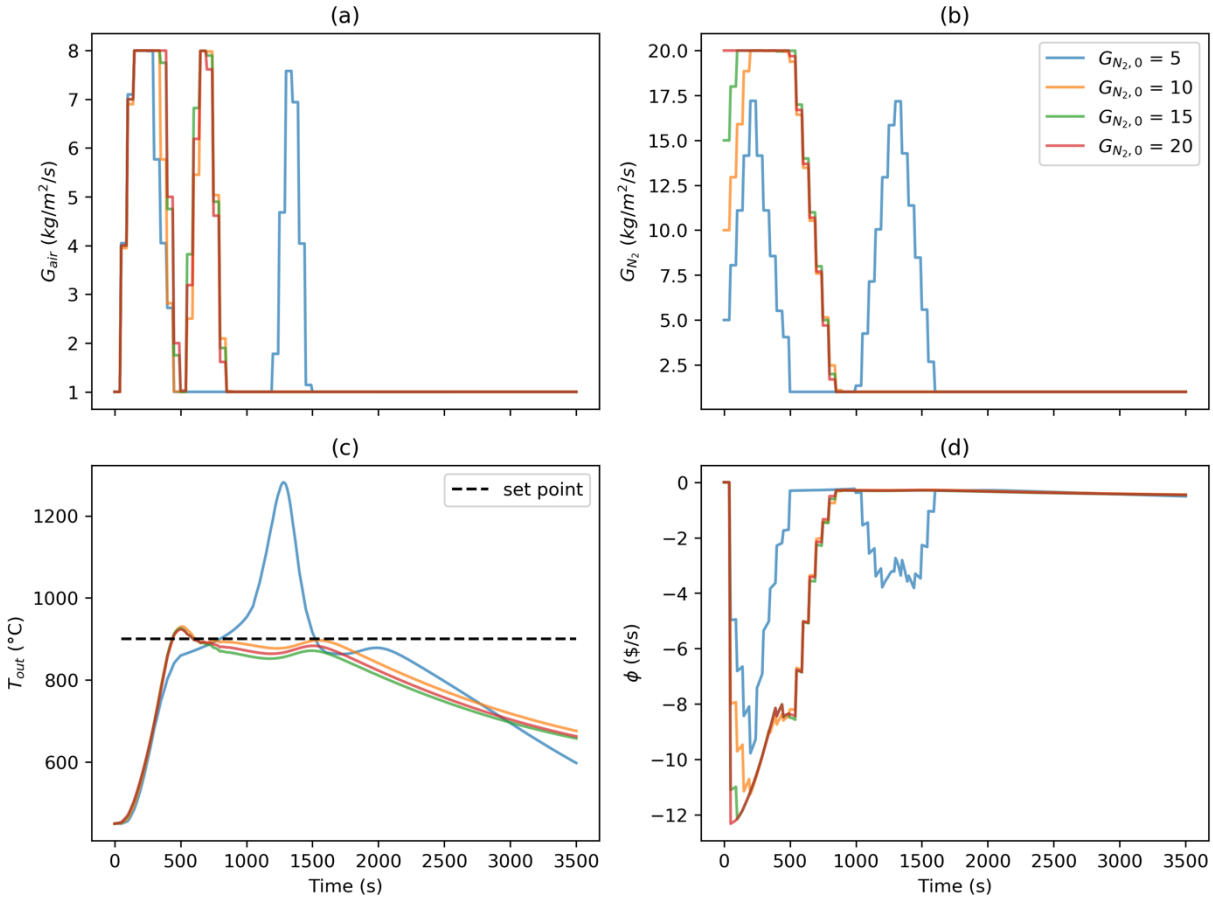

Figure 4: Trajectories for varying initial inert flux at Ontario mid-peak energy prices obtained using the NMPC by Toffolo et al. [32].

In contrast to the NMPC, the EMPC can achieve revenues in most of the inert inlet cases (Table 3). In the high initial inert case, the maximization of temperature is not enough to offset the initial consumption of N_2 given the low price of energy. However, when the initial inert inlet is lower, the profit rates dominate the expense rates (Figure 5d). In all initial inert flux cases, the air flux is initially maximized before a decrease towards the end of the stage (Figure 5a); this serves to increase the throughput of the system so that more energy is routed to the downstream turbine when the unit is hot (Figure 5c). Further, all EMPC cases minimized the usage of inert (Figure 5b) as it not an economical way to increase the system throughput. Lower initial inert fluxes are also observed to lead to prolonged period of peak temperature (Figure 5c) as the air to inert ratio is more quickly increased thereby increasing the rate of combustion. This also leads to shortened periods of air inlet (Figure 5a) and quicker settling to a cold temperature regime (Figure 5c) such that the stage could be shortened, thus further intensifying the production of energy in CLC. The shortened stage time is particularly salient with respect to the NMPC, which continues cooling even at the end of the simulated time (Figure 4c).

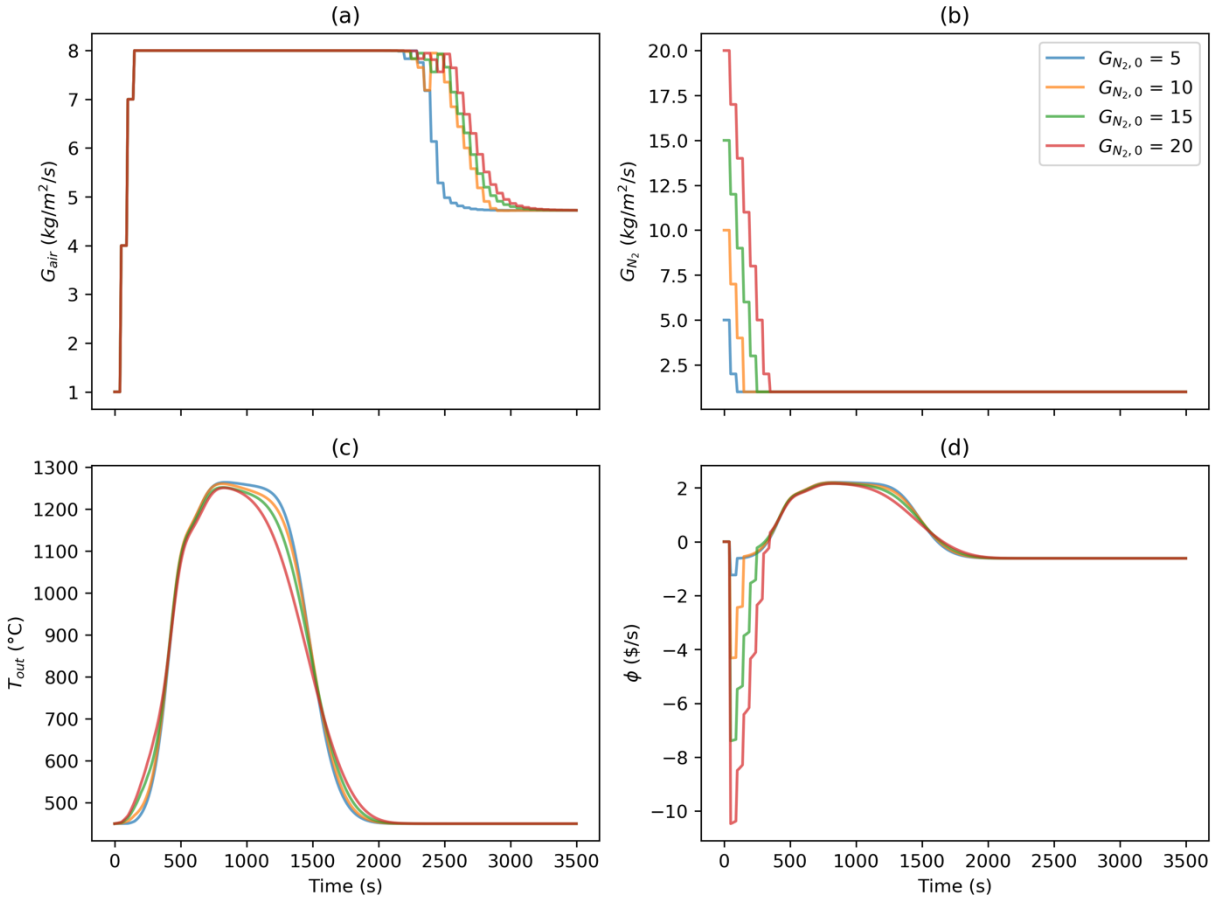

Figure 5: Trajectories for varying initial inert flux at Ontario mid-peak energy prices obtained using the EMPC proposed herein.

Despite the improvement in performance using the EMPC over the NMPC, the revenues remain modest (Table 3); this is owed to the low relative price of energy with respect to the inert, which means that the potential for high profits is reduced.

4.1.2. Energy price variation

While the previous scenario tests the controllers on the oxidation stage assuming Ontario mid-peak energy rates [26], this was only shown to lead to modest revenues. In jurisdictions with higher energy prices (e.g., the United Kingdom), CLC has the potential to be more profitable. As per the UK Department of Energy Security & Net Zero, the cap for energy in the UK is $P_e = 0.277\ £GBP/kWh = 0.45\ \$CAD/kWh$ [43]. Accordingly, a sensitivity analysis is performed on operated PBR CLC from the Ontario off-peak price to the UK price cap; this is summarized in Table 4.

Table 4: Cumulative revenue and peak temperature for varying energy prices at $G_{N_2} = 5\ kg/m^2/s$.

$\boldsymbol{P_e}(\$\boldsymbol{CAD/kWh})$	0.087	0.122	0.182	0.25	0.30	0.35	0.40	0.45
$\boldsymbol{R_{ox,EMPC}}$ $(\$\boldsymbol{CAD/stage})$	−9.72	858.17	2346.01	4032.21	4740.71	5646.15	6805.05	7816.04
$\boldsymbol{T_{max,EMPC}}$ $(°\boldsymbol{C})$	1264	1264	1264	1264	1275	1284	1285	1291

$\boldsymbol{R_{ox,NMPC}}$ ($\$CAD/stage$)	-5714.13	-4868.37	-3418.48	-1775.28	-567.04	641.20	1849.44	3057.68

As expected, there is a trend of increasing revenues with increasing electricity price as the energy produced by the CLC can be sold for more; this is also owed to the peak temperature increasing with electricity price. The EMPC outperforms the NMPC on all cases, whereby the NMPC is only profitable with $P_e \geq 0.35\ \$CAD/kWh$ because of its low temperature set point. In the EMPC case, the system reaches higher temperatures so that more energy is produced by the CLC; this is also shown in Figure 6c for energy price cases between the Canadian on-peak and the UK price cap.

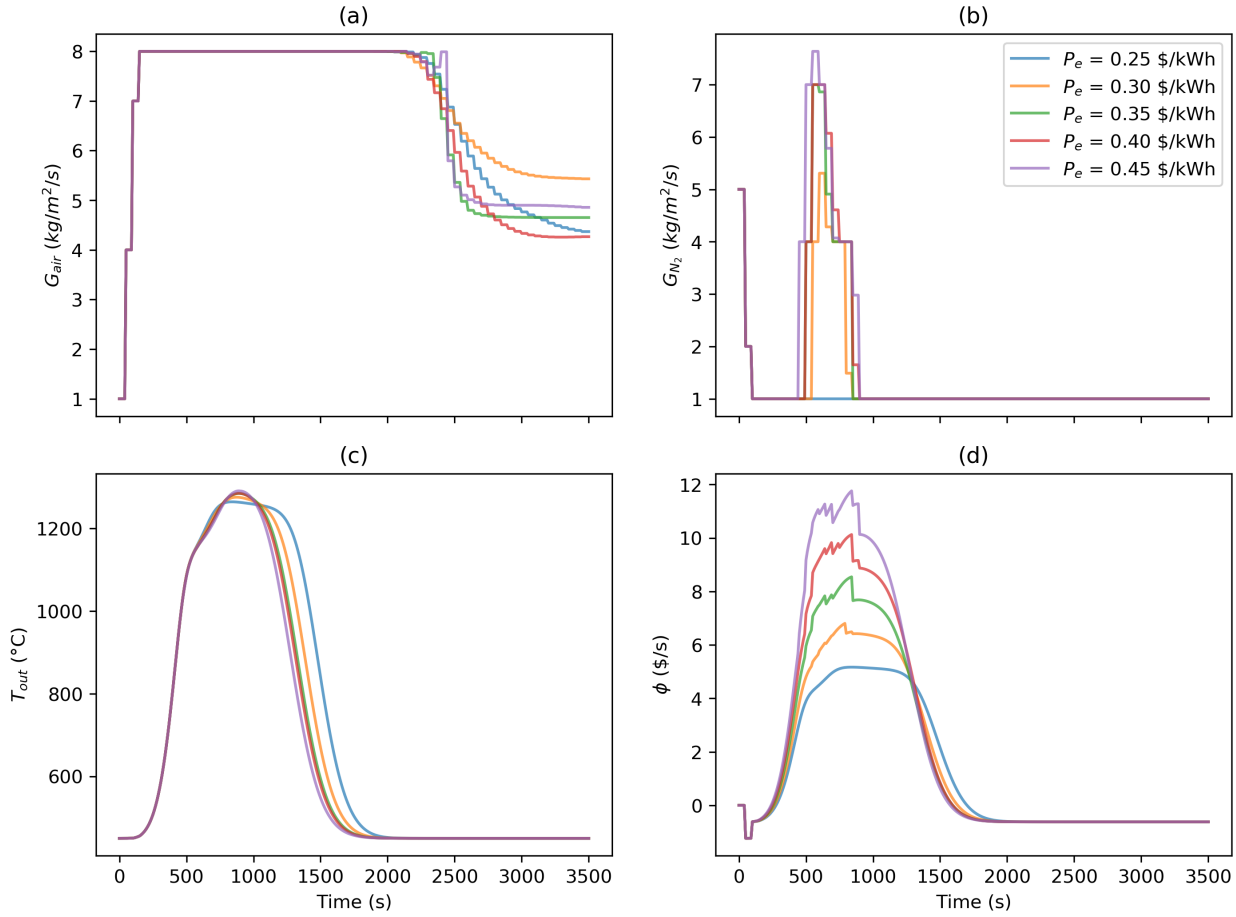

Figure 6: Trajectories for varying energy prices at $G_{N_2} = 5\ kg/m^2/s$ obtained using the EMPC proposed herein.

The increased CLC temperature is caused by the peaking behaviour in the inert inlet (Figure 6b). In contrast to cases with low energy prices ($P_e < 0.3\ \$CAD/kWh$), scenarios with high energy prices are incentivized to input inert as the temperature is rising; this is done as the air inlet (Figure 6a) is quickly saturated, thus the only way to increase throughput (and thus reaction rate) is through the expensive inert. Despite the price of N_2, high energy prices justify increased consumption as shown in Figure 6d whereby profit rate peaks are observed to correspond to the periods of peak temperature. Through these maximized profit profiles, the stage revenues summarized in Table 4 are achieved such that the EMPC-operated system is further intensified under different price scenarios.

4.2. Reduction stage

As the reduction stage is tasked with regenerating the OC through combustion; the main variables of interest are the fuel consumption and the CO_2 produced. Each CLC reduction stage is run for $t_f = 1500\,s$ such that peak CO_2 selectivity can be achieved, followed by a decrease in reaction efficiency. The average EMPC CPU time for this stage was $17.8\,s$, which is less than the sampling interval length (Table 2); accordingly, the controller is fit for online use. In addition to stage revenue (R_{red}) and CO_2 throughput ($G_{CO_2,out}$), the reduction stage is assessed in terms of its CO_2 selectivity S_{CO_2} (mol/mol), which quantifies its fuel efficiency.

4.2.1. Ratcheting carbon prices

Many jurisdictions have adopted a "ratcheting" approach to carbon pricing to ease the transition into more stringent emissions penalties. For instance, Canada [29] is increasing its carbon price by $15\ \$CAD/tn$ from a current price of $65\ \$CAD/tn$ in 2023 to a final price of $170\ \$CAD/tn$ in 2030; this range in line with prices in other advanced economies [44]. The reduction stage in the PBR CLC is subject to these carbon tax changes such that it may affect its economically optimal operation; this is shown in Table 5 (note that the CLC behaviour does not change with prices past $155\ \$CAD/tn$, hence the omission of $170\ \$CAD/tn$ from the table; this occurs as a minimum selectivity is reached past this price).

Table 5: Cumulative revenue and peak CO_2 selectivity for varying carbon prices at $P_{CH_4} = 0.2\ \$CAD/m^3$ [30] and $P_{sep} = 2.37\ \$CAD/mscf$ [31].

$\boldsymbol{P_{CO_2}(\$CAD/tn)}$	65	80	95	110	125	140	155
$\boldsymbol{R_{red,EMPC}}$ $(\$CAD/stage)$	−546.96	−355.04	−189.96	40.17	319.94	626.76	906.21
$\boldsymbol{S_{CO_2,max,EMPC}}$ (mol/mol)	0.83	0.83	0.67	0.53	0.45	0.40	0.39
$\boldsymbol{R_{red,NMPC,selec}}$ $(\$CAD/stage)$	−617.22	−412.98	−208.74	−4.49	199.75	403.99	608.23
$\boldsymbol{R_{red,NMPC,util}}$ $(\$CAD/stage)$	−622.61	−405.49	−208.37	−1.25	205.87	412.99	620.11

Toffolo et al. [32] previously proposed two set point targets for the CLC NMPC deployed in the reduction stage, wherein CO_2 selectivity and CH_4 utilization are prioritized, respectively; the cumulative revenue for both is shown in Table 5 with the subscripts $selec$ and $util$. All carbon price instances of the EMPC outperform all instances of the NMPC, irrespective of whether the selectivity or utilization target is used on the latter; this is manifested through the EMPC achieving better stage economics in situations of both cost saving and profit maximization. Toffolo et al. [32] had previously noted that the CLC system exhibits a trade-off between outlet CO_2 purity and flux whereby the optimal balance between the two goals was not explicitly solved for. This trade-off is owed to an increased amount of unreacted methane and other by-products (e.g., H_2) when throughput is prioritized, which dilutes the outlet CO_2 purity. The EMPC proposed herein provides an optimal way to balance these two goals from an economic perspective, hence it provides an economic advantage that amounts to further intensification.

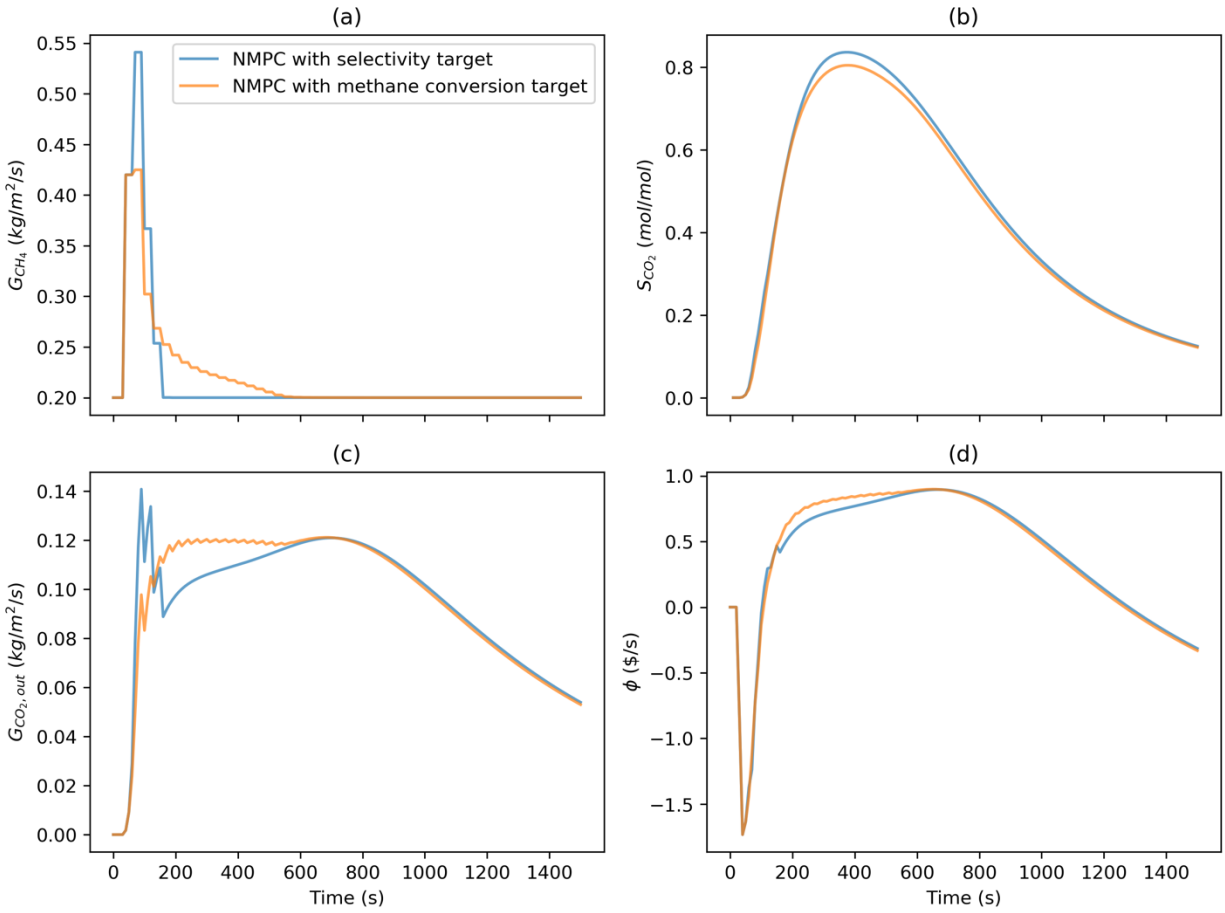

Figure 7: Trajectories obtained using the NMPC proposed by Toffolo et al. [32]. Prices calculated at $P_{CO_2} = 155\ \$CAD/m^3$, $P_{CH_4} = 0.2\ \$CAD/m^3$ [30], and $P_{sep} = 2.37\ \$CAD/mscf$ [31].

Figure 7 shows the reduction stage behaviour under the objectives from Toffolo et al. [32]. Both objectives impose an initial peak in methane inlet (Figure 7a), whereby the flow is subsequently gradually decreased to its lower bound. This causes a delayed peaking behaviour in the CO_2 selectivity (Figure 7b) in which a maximum of $\sim 0.8\ mol/mol$ is reached for both objectives. In terms of outlet CO_2 flux, the initial inlet causes high initial outlet, followed by a second delayed outlet peak once the reduction reaction begins taking place (Figure 7c). For the carbon price of $155\ \$CAD/tn$ as used for Figure 7d, the reduction stage is able to make a revenue as shown in Table 5; however, this is at least $\sim 33\%$ less that when the EMPC is used. Further, with a carbon price of $110\ \$CAD/tn$, the EMPC can make a slight revenue while the NMPCs result in losses. Below this carbon price ($< 110\ \$CAD/tn$), all control schemes result in losses whereby the EMPC is best able to minimize the loss. Despite these potential losses, the reduction stage should still be performed as it is inherently a recovery phase that must be executed to enable the profitable oxidation stage; this trade-off is discussed in a later section.

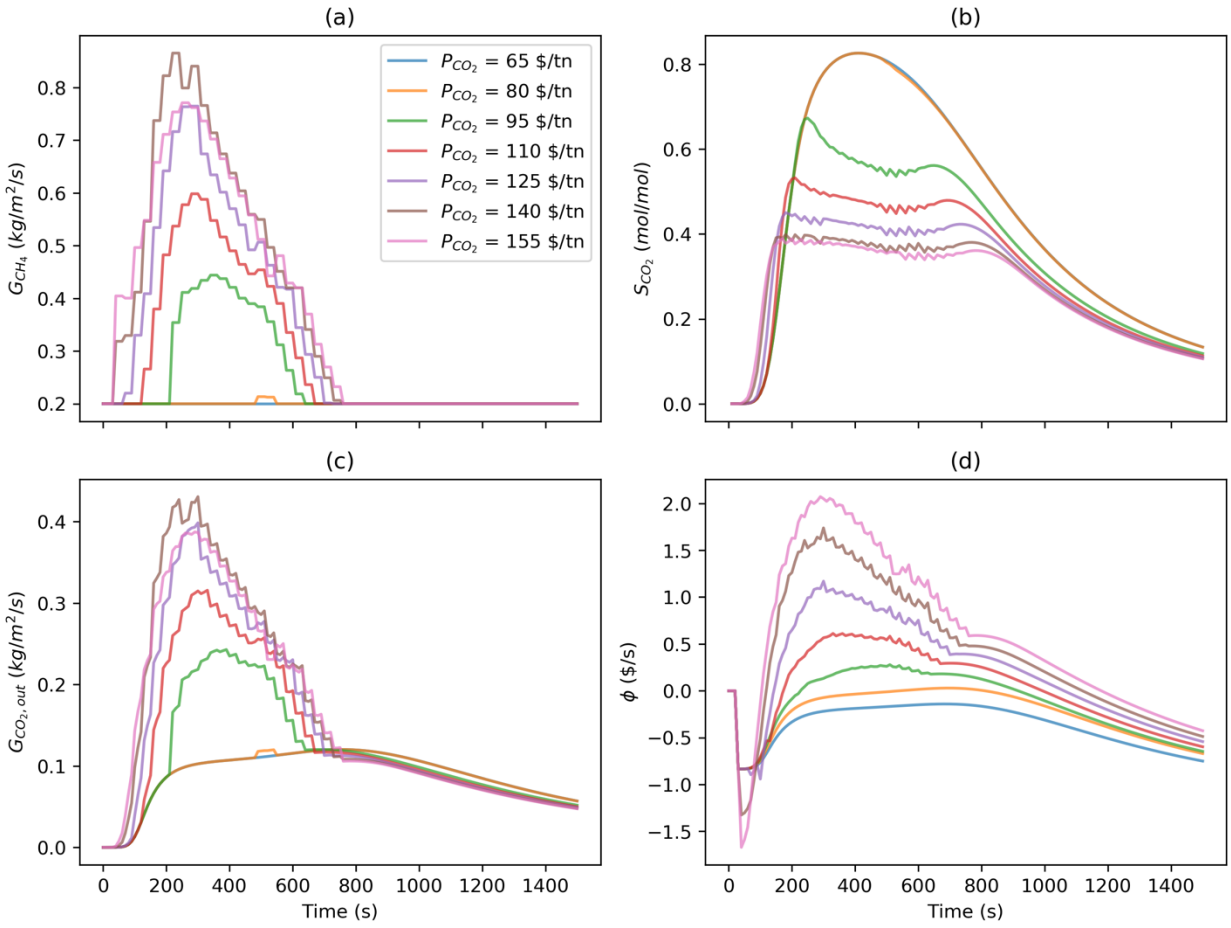

Figure 8: Trajectories obtained using the EMPC proposed herein for varying carbon prices, $P_{CH_4} = 0.2\ \$CAD/m^3$ [30], and $P_{sep} = 2.37\ \$CAD/mscf$ [31].

Figure 8 shows the EMPC trajectories for different carbon prices wherein the trade-off between purity and throughput can be observed using the balancing mechanism of the carbon price. For low carbon prices ($\leq 80\ \$CAD/tn$), the inlet (Figure 8a) is effectively kept at its lower bound since the methane price dominates the objective function; this results in high CO_2 selectivity (Figure 8b) and low throughput (Figure 8c). As carbon price increases beyond 80 $\$CAD/tn$, each higher carbon price has a larger methane inlet peak that occurs sooner and lasts longer (Figure 8a). This increased methane inlet results in decreasing CO_2 selectivity (Figure 8b) and increasing throughput (Figure 8c). In general, the objective used in the EMPC maximizes CO_2 outlet flux using its carbon price term (equation (4)); this flux is best increased by throughput as selectivity cannot increase beyond $\sim 0.83\ mol/mol$ as shown in Table 5. Despite this increased CO_2 flux seeming like a potentially perverse incentive, it benefits the overall CLC process. More CO_2 production entails that there is a greater extent of reduction in the OC, thus it will have better performance when used in the oxidation stage. Even though constant stage times were used in the present study, quicker reduction could also potentially enable shorter stage times. In a scheduling context, if the relative amount of oxidation time to reduction time can be shifted more towards oxidation, then more energy can be generated in time. Moreover, as CO_2 utilization [45] becomes a more mature industry, the increased reduction CO_2 flux could yield potentially higher profits.

4.2.2. Fuel price effect

In addition to gradually increasing carbon prices, the price of natural gas may vary such that it can impact the economic operation of CLC. Accordingly, the CLC EMPC is deployed for 155 $\$CAD/tn$ at varying natural gas prices as shown in Figure 9. The minimum gas price is assumed to be near the Canadian nominal price [30] of 0.2 $\$CAD/m^3$ and this price is increased until trajectory changes are no longer observed (at ~ 0.45 $\$CAD/m^3$); however, gas prices in some jurisdictions can exceed this upper limit [46]. The main point of note is that fuel prices have the inverse effect on the EMPC with respect to carbon prices; this is reflected in higher selectivity (Figure 9b) and lower throughput (Figure 9c) with increasing fuel prices, which occur as increasingly expensive gas causes lower feed (Figure 9a). Further, expensive gas can make the process very costly as reflect in Figure 9d, whereby losses are incurred for much of the trajectories with higher prices.

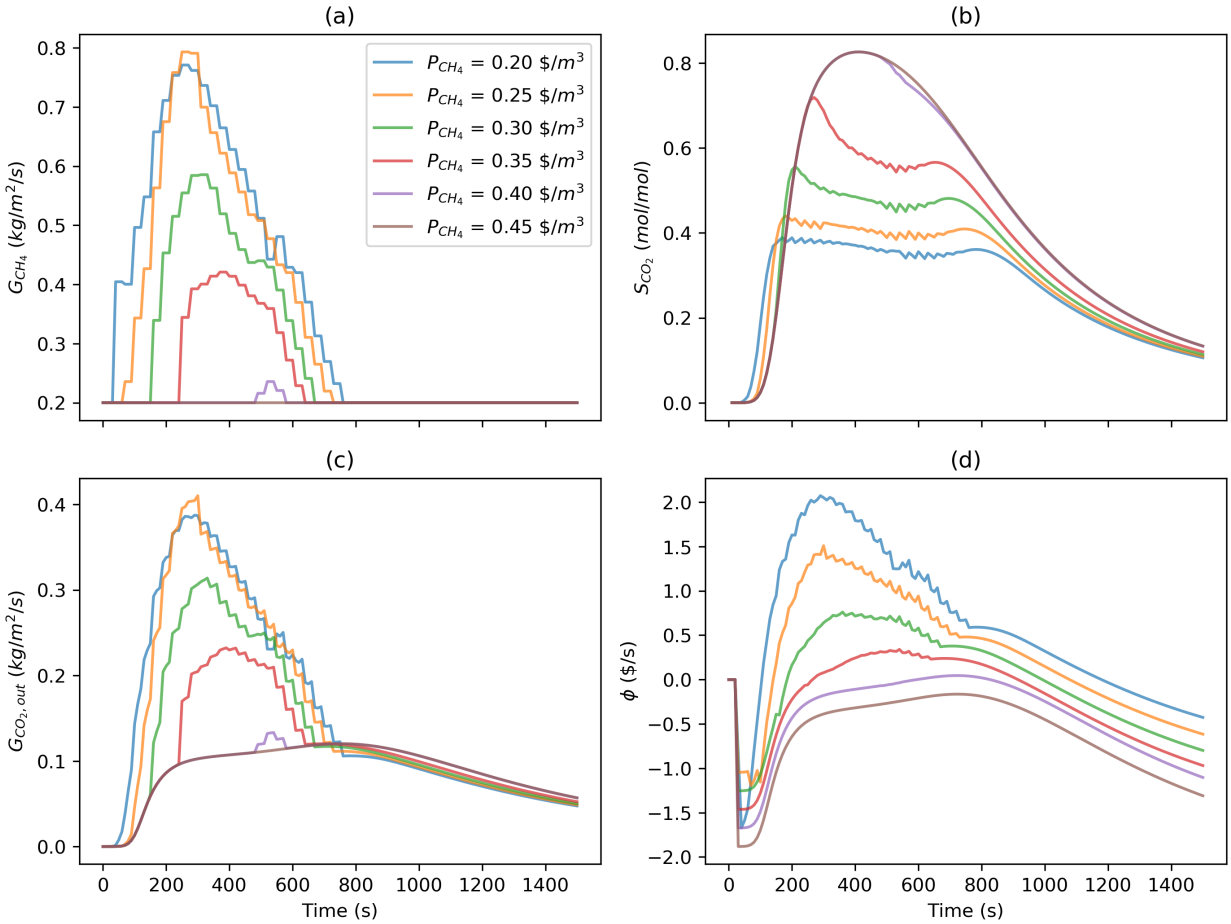

Figure 9: Trajectories obtained using the EMPC proposed herein for varying natural gas prices, $P_{CO_2} = 155$ $\$CAD/tn$ [29], and $P_{sep} = 2.37$ $\$CAD/mscf$ [31].

As the inverse effect of carbon and fuel prices was observed, a further sensitivity analysis was performed while simultaneously varying both incentives; this is summarized in Figure 10. Generally, the CO_2 selectivity is maximized similarly to the high fuel price cases shown in Figure 9a; this behaviour is not observed when the fuel prices are low and the carbon prices are high (Figure 10a). The throughput behaviour is inversely correlated to the selectivity behaviour (Figure 10b) whereby low flux is observed as in the high fuel price cases in Figure 9b; this throughput is

accordingly increased only in the high carbon price and low fuel price regime. On aggregate, the fuel and carbon prices manifest their influence through the selectivity-throughput trade-off; low fuel prices (conversely, high carbon prices) are met by increasing throughput as selectivity peaks at $\sim 0.83\ mol\ CO_2/mol\ CH_4$. Beyond this point of maximum selectivity, the best policy is to increase the total outlet flowrate with lower carbon conversion as the total carbon output can only be increased by processing more fuel. Despite other by-products (e.g., H_2) being produced with higher throughput, the total amount of carbon in the outlet is increased on aggregate by having a more carbon-dilute gas with a larger flowrate (e.g., the selectivity is halved while the throughput is increased fourfold when comparing edge cases in Figure 10). In contrast, the opposite effect is observed with high fuel and low carbon prices, whereby selectivity is prioritized at the expense of throughput.

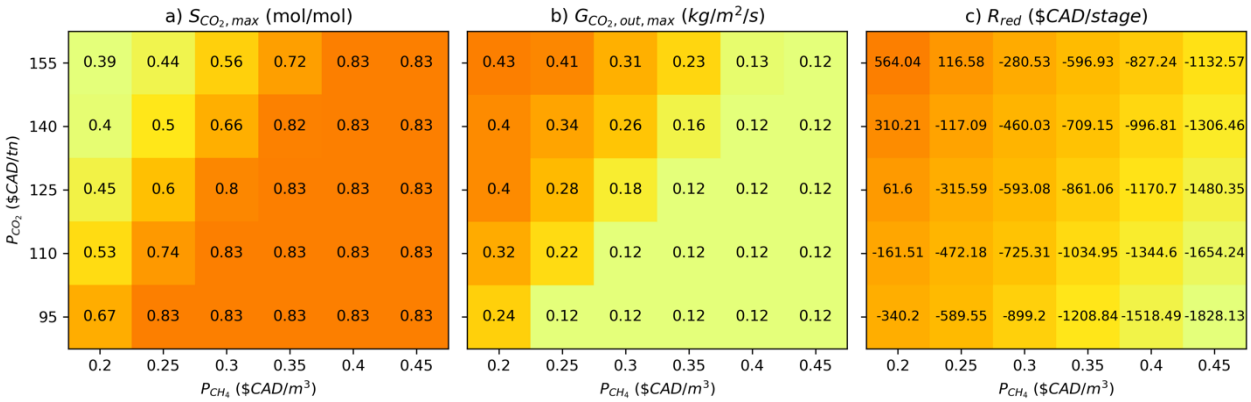

Figure 10: Joint sensitivity analysis for EMPC-operated system with varying CO_2 prices (y-axes) and natural gas prices (x-axes); a) CO_2 selectivity, b) CO_2 throughput, c) stage revenue.

In terms of economics (Figure 10c), the EMPC is almost always aiming to minimize losses, leading to a cost of CO_2 avoided, which is natural for CCS systems [47]. Losses imply that the carbon avoided by the CLC system is not sufficiently high to offset the natural gas price; as the reduction stage is mainly a regeneration stage for the OC, this is expected. In comparison to the potential stage revenue from the oxidation stage, these losses are relatively minor (especially when energy prices are high); accordingly, this cost is acceptable. In cases of high carbon prices and low fuel prices, there is a positive revenue. Note that this is not actually a revenue made; rather, a positive economic gain *relative* to a technology that would be emitting its CO_2. Nonetheless, as shown in the previous section, the EMPC herein is shown to optimize these oxidation economics relative to the NMPC.

4.3. Overall stage performance

When jointly considering the economics of both the oxidation and reduction stages within the EMPC-operated PBR CLC process, guidelines for the operation of CLC can be established for varying economic incentives. Figure 11 shows sensitivity of overall process revenue (R_{CLC}) to the price variations previously tested with $G_{N_2,0} = 5\ kg/m^2/s$ in the oxidation stage. It is important to recognize that, while the revenue of the CLC operation is dependent on these prices, they are exogeneous signals, which are effectively out of the control of operators. However, by creating a look-up table such as that shown in Figure A12 (Appendix), decision-makers can decide if conditions are suitable for deploying the CLC by establishing economic thresholds that warrant operation. In this way, the CLC can be used intermittently when economic conditions are favourable. As indeed any CLC process is inherently intermittent owed

to its need for stage-wise operation, decisions on whether to execute or delay a stage can be made respect to the current market prices by determining the expected revenue as predicted in Figure A12 (Appendix) and whether it meets a user-defined threshold for operation.

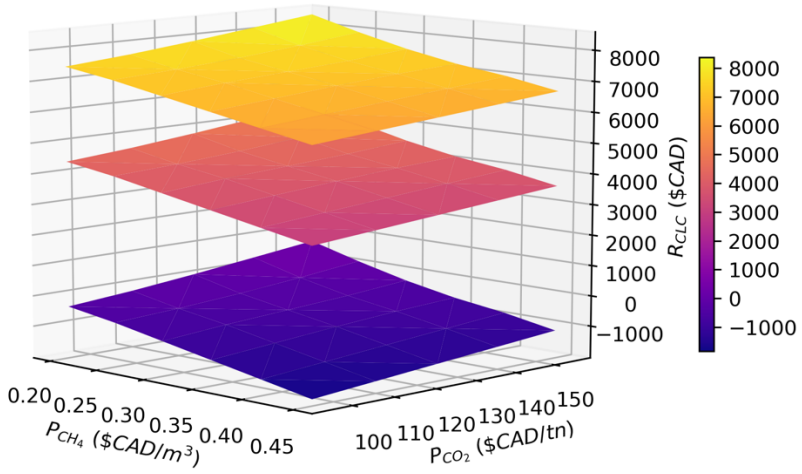

Figure 11: EMPC-operated revenue surfaces (R_{CLC}, z-axis) with varying CO_2 prices (y-axes), natural gas prices (x-axes). Bottom surface uses $P_e = 0.087\ \$CAD/kWh$, middle surface uses $P_e = 0.3\ \$CAD/kWh$, and top surface uses $P_e = 0.45\ \$CAD/kWh$.

Figure 11 shows the aggregate results of the price effects explored in the previous sections as follows: increasing revenue with increasing energy prices (i.e., in higher surfaces), decreasing revenue with increasing methane prices (i.e., when moving right on the x-axis), and increasing revenue with increasing carbon prices (i.e., when right on the y-axis). The sensitivity to the energy price is most pronounced, which is in line with the fact that the CLC process' main objective is to generate energy; accordingly, it is the factor that effectively determines whether the overall process is profitable. Figure 11 also shows that the CLC is often not profitable for low energy prices (also shown in more detail in Figure A12, Appendix), regardless of the methane and carbon prices. With higher energy prices ($\geq 0.182\ \$CAD/kWh$), the CLC process always becomes a profitable proposition, with very high cycle revenues in the high energy price regime.

The trend of increasing revenue with high carbon prices and low methane prices, as observed in section 4.2.2., is preserved even when varying energy prices. The sensitivity to methane prices appears to be the second most significant economic factor, where it has an influence on the revenue of each stage through the expense that is incurred; in the high energy price regime (e.g., Figure 11 top plot), a low methane price can increase revenues by up to $\sim 25\%$. Lastly, the carbon price appears to have the least effect on revenue as it is effectively an unwanted by-product of the CLC process; in the high energy price regime, changing carbon prices are only able to increase revenues by $\sim 12\%$.

5. Conclusions

CLC has been designed to produce energy with inherent carbon capture. The PBR configuration of CLC employs process intensification by performing both CLC stages within the same vessel. The work presented herein proposes an EMPC scheme to further improve the performance of CLC, enabled by a pseudo-homogeneous process model used in the controller. Economic functions are proposed for both oxidation and reduction stages where, respectively, the

energy generation and fuel management are dynamically optimized. Additionally, the online application of EMPC can accommodate for inter-stage changes in economic incentives. The EMPC is stated generally as to apply to any CLC configuration but tested on the PBR design, where it is found to provide economic benefit with respect to the state-of-the-art regulatory controller. The oxidation stage EMPC provides an order-of-magnitude economic improvement while the reduction stage EMPC yielded up to ~33% improvement over previous NMPC implementations with set point tracking objectives that may not lead to an economically optimal operation. Moreover, the reaction time in both stages was shortened thus further intensifying the unit with faster processing times leading to higher potential productivity. The economics of oxidation were found to be highly dependent on the initial inert flux and the energy sales price, whereby the EMPC maximized the peak outlet temperature to increase the energy output under varying market conditions. Further, the reduction stage was found to be highly sensitive to both carbon and fuel prices with inverse effect. High fuel prices were found to result in high CO_2 selectivity and low throughput while high carbon prices increased throughput at the expense of selectivity. On aggregate, the amount of fuel being processed was higher in these low fuel price and high carbon price conditions where the use of CLC is beneficial with respect to traditional methods of energy generation owed to its inherent carbon capture. Considering both stage economics jointly, the EMPC-operated PBR CLC can generate revenue in all cases provided that the sales prices of energy is greater than or equal to the Ontario on-peak price. Price-dependent deployment of CLC is suggested, which agrees with the inherently intermittent operation of the process, which should be deployed when economic conditions are favourable to the operators.

Batch-to-batch scheduling considering several CLC units, the effect of processing time [48], and planning decisions [49] remain to be addressed; while out of the scope of the present study, these approaches can be integrated with model-based control [50] to accommodate diurnal energy demands. As illustrated in this work, the EMPC approach can shorten the batch time in both stages; future works could explore the effect of stage timings by jointly considering real-time control with long-term scheduling decisions. By embedding a control scheme within a scheduling problem, the intermittent operation of CLC can be optimally timed to maximize energy generation or profit, which has been shown to result in significant benefits for conventional CCS plants (e.g., [51]). Moreover, the main assumption made herein is that of full state accessibility by the controller, which requires significant investment in instrumentation. To alleviate this, other CCS processes have deployed model-based (e.g., moving horizon estimation [4, 52, 53]) as well as data-driven (e.g., multi-layer perceptron based extended Kalman filter [54]) approaches. Similar strategies could provide realistic predictions of the expected closed-loop behaviour of CLC to deploy state-of-the-art control systems without requiring expensive instrumentation.

Acknowledgements

The authors would like to acknowledge the Natural Sciences and Engineering Research Council of Canada (NSERC) for their financial support.

References

[1] International Energy Agency (IEA), 2022. World Energy Outlook 2022. https://www.iea.org/reports/world-energy-outlook-2022 (accessed 2 October 2023).

[2] International Energy Agency (IEA), 2023. Outlooks for gas markets and investment. https://www.iea.org/reports/outlooks-for-gas-markets-and-investment (accessed 2 October 2023).

[3] A.I. Osman, M. Hefny, M.I.A. Abdel Maksoud, A.M. Elgarahy, D.W. Rooney, 2021. Recent advances in carbon capture storage and utilisation technologies: a review. *Environ. Chem. Lett*., 19, 797–849. https://doi.org/10.1007/s10311-020-01133-3.

[4] G.D. Patrón, L. Ricardez-Sandoval, 2022. An integrated real-time optimization, control, and estimation scheme for post-combustion CO_2 capture. *Appl. Energy*, 308, 118302. https://doi.org/10.1016/j.apenergy.2021.118302.

[5] S. Abuelgasim, W. Wang, A. Abdalazeez, 2021. A brief review for chemical looping combustion as a promising CO2 capture technology: Fundamentals and progress. *Sci. Total Environ*., 764, 142892. https://doi.org/10.1016/j.scitotenv.2020.142892.

[6] S. Noorman, M. van Sint Annaland, H. Kuipers, 2007. Packed Bed Reactor Technology for Chemical-Looping Combustion. *Ind. Eng. Chem. Res*., 46, 4212–4220. https://doi.org/10.1021/ie061178i.

[7] L. Han, Z. Zhou, G.M. Bollas, 2013. Heterogeneous modeling of chemical-looping combustion. Part 1: Reactor model. *Chem. Eng. Sci.,* 104, 233–249. https://doi.org/10.1016/j.ces.2013.09.021.

[8] H.P. Hamers, F. Gallucci, G. Williams, M. van Sint Annaland, 2015. Experimental demonstration of CLC and the pressure effect in packed bed reactors using $NiO/CaAl_2O_4$ as oxygen carrier. *Fuel*, 159, 828–836. https://doi.org/10.1016/j.fuel.2015.07.034.

[9] H. Gu, L. Shen, J. Xiao, S. Zhang, T. Song, 2011. Chemical Looping Combustion of Biomass/Coal with Natural Iron Ore as Oxygen Carrier in a Continuous Reactor. *Energy Fuels*, 25, 446–455. https://doi.org/10.1021/ef101318b.

[10] H.R. Kim et al., 2013. Coal direct chemical looping combustion process: Design and operation of a 25-kWth sub-pilot unit. *Fuel*, 108, 370–384. https://doi.org/10.1016/j.fuel.2012.12.038.

[11] X. Wang, X. Wang, Y. Shao, B. Jin, 2020. Coal-fueled separated gasification chemical looping combustion under autothermal condition in a two-stage reactor system. *Chem. Eng. J*., 390, 124641. https://doi.org/10.1016/j.cej.2020.124641.

[12] T. Wanotayaroj, B. Chalermsinsuwan, P. Piumsomboon, 2020. Dynamic simulation and control system for chemical looping combustion. *Energy Rep*., 6(2), 32–39. https://doi.org/10.1016/j.egyr.2019.11.038.

[13] M. Lucio, L. Ricardez-Sandoval, 2020. Dynamic modelling and optimal control strategies for chemical-looping combustion in an industrial-scale packed bed reactor. *Fuel*, 262, 116544. https://doi.org/10.1016/j.fuel.2019.116544.

[14] R.B. Parker, L.T. Biegler, 2022. Dynamic Modeling and Nonlinear Model Predictive Control of a Moving Bed Chemical Looping Combustion Reactor. *IFAC-PapersOnLine*, 55(7), 400–405. https://doi.org/10.1016/j.ifacol.2022.07.476.

[15] K. Toffolo, L. Ricardez-Sandoval, 2021. Optimal Design and Control of a Multiscale Model for a Packed Bed Chemical-Looping Combustion Reactor. *IFAC-PapersOnLine*, 54(3), 615–620. https://doi.org/10.1016/j.ifacol.2021.08.310.

[16] L. Han, G.M. Bollas, 2016. Dynamic optimization of fixed bed chemical-looping combustion processes. *Energy*, 112, 1107–1119. https://doi.org/10.1016/j.energy.2016.07.031.

[17] C.O. Iloeje, Z. Zhao, A.F. Ghoniem, 2018. Design and techno-economic optimization of a rotary chemical looping combustion power plant with CO2 capture. *Appl. Energy*, 231, 1179–1190. https://doi.org/10.1016/j.apenergy.2018.09.058.

[18] C.O. Okoli et al., 2020. A framework for the optimization of chemical looping combustion processes. *Powder Technol*., 365, 149–162. https://doi.org/10.1016/j.powtec.2019.04.035.

[19] S. Noorman, F. Gallucci, M. van Sint Annaland, J.A.M. Kuipers, 2011. A theoretical investigation of CLC in packed beds. Part 1: Particle model. *Chem. Eng. J*., 167(1), 297–307. https://doi.org/10.1016/j.cej.2010.12.068.

[20] S. Noorman, F. Gallucci, M. van Sint Annaland, J.A.M. Kuipers, 2011. A theoretical investigation of CLC in packed beds. Part 2: Reactor model. *Chem. Eng. J*., 167(1), 369–376. https://doi.org/10.1016/j.cej.2011.01.012.

[21] L. Han, Z. Zhou, G.M. Bollas, 2013. Heterogeneous modeling of chemical-looping combustion. Part 2: Particle model. *Chem. Eng. Sci.,* 113, 116–128. https://doi.org/10.1016/j.ces.2014.03.030.

[22] M. Ellis, H. Durand, P.D. Christofides, 2014. A tutorial review of economic model predictive control methods. *J. Process Control*, 24(8), 1156–1178. https://doi.org/10.1016/j.jprocont.2014.03.010.

[23] J.G. Segovia-Hernández, S. Hernández, E. Cossío-Vargas, E. Sánchez-Ramírez, 2023. Challenges and opportunities in process intensification to achieve the UN's 2030 agenda: Goals 6, 7, 9, 12 and 13. *Chem. Eng. Process*., 192, 109507. https://doi.org/10.1016/j.cep.2023.109507.

[24] Y. Tian, S.E. Demirel, M.M. Faruque Hassan, E.N. Pistikopoulos, 2018. An overview of process systems engineering approaches for process intensification: State of the art. *Chem. Eng. Process*., 133, 160–210. https://doi.org/10.1016/j.cep.2018.07.014.

[25] E.N. Pistikopoulos, Y. Tian, R. Bindlish, 2021. Operability and control in process intensification and modular design: Challenges and opportunities. *AIChE J*., 67(5), e17204. https://doi.org/10.1002/aic.17204.

[26] Ontario Energy Board (OEB). Electricity rates. https://www.oeb.ca/consumer-information-and-protection/electricity-rates (accessed 29 September 2023).

[27] V. Spallina, M.C. Romano, P. Chiesa, F. Gallucci, M. van Sint Annaland, G. Lozza, 2014. Integration of coal gasification and packed bed CLC for high efficiency and near-zero emission power generation. *Int. J. Greenh. Gas Control*, 27, 28–41. https://doi.org/10.1016/j.ijggc.2014.04.029.

[28] Intratec. Nitrogen Gas Price | Current and Forecast. https://www.intratec.us/chemical-markets/nitrogen-gas-price (accessed 29 September 2023).

[29] Environment Change and Climate Canada, 2020. A healthy environment and a healthy economy. https://www.canada.ca/en/environment-climate-change/news/2020/12/a-healthy-environment-and-a-healthy-economy.html (accessed 26 October 2023).

[30] Ontario Energy Board (OEB). Natural gas rates. https://www.oeb.ca/consumer-information-and-protection/natural-gas-rates (accessed 29 September 2023).

[31] M. Hoorfar, Y. Alcheikhhamdon, B. Chen, 2018. A novel tool for the modeling, simulation and costing of membrane based gas separation processes using Aspen HYSYS: Optimization of the CO_2/CH_4 separation process. *Comput. Chem. Eng*., 117, 11–24. https://doi.org/10.1016/j.compchemeng.2018.05.013.

[32] K. Toffolo, S. Meunier, L. Ricardez-Sandoval, 2023. Optimal operation of a large-scale packed bed chemical-looping combustion process using nonlinear model predictive control. *Fuel*, 357(B), 129876. https://doi.org/10.1016/j.fuel.2023.129876.

[33] R.G. Rice and D.D. Do, 1995. Solution Techniques for Models Yielding Ordinary Differential Equations (ODE). *Applied Mathematics and Modeling for Chemical Engineers*, Toronto, John Wiley & Sons, pp. 37–103.

[34] H. Jin, M. Ishida, 2002. Reactivity Study on Natural-Gas-Fueled Chemical-Looping Combustion by a Fixed-Bed Reactor. *Ind. Eng. Che. Res*., 41(16), 4004–4007. https://doi.org/10.1021/ie020184l.

[35] V. Spallina, B. Marinello, F. Gallucci, M.C. Romano, M. van Sint Annaland, 2017. Chemical looping reforming in packed-bed reactors: Modelling, experimental validation and large-scale reactor design. *Fuel Process. Technol.,* 156, 156–170. https://doi.org/10.1016/j.fuproc.2016.10.014.

[36] G. Diglio, P. Bareschino, E. Mancusi, F. Pepe, 2018. Techno-Economic Evaluation of a Small-Scale Power Generation Unit Based on a Chemical Looping Combustion Process in Fixed Bed Reactor Network. *Ind. Eng. Chem. Res*., 57(33), 11299–11311. https://doi.org/10.1021/acs.iecr.8b02378.

[37] Z. Zhou, L. Han, G.M. Bollas, 2014. Kinetics of NiO reduction by H2 and Ni oxidation at conditions relevant to chemical-looping combustion and reforming. *Int. J. Hydrog. Energy*, 39(16), 8535–8556. https://doi.org/10.1016/j.ijhydene.2014.03.161.

[38] O. Nordness, L. Han, Z. Zhou, G.M. Bollas, 2016. High-Pressure Chemical-Looping of Methane and Synthesis Gas with Ni and Cu Oxygen Carriers. *Energy Fuels*, 30(1), 504–514. https://doi.org/10.1021/acs.energyfuels.5b01986.

[39] I. Iluita, R. Tahoces, G.S. Patience, S. Rifflart, F. Luck, 2010. Chemical-Looping Combustion Process: Kinetics and Mathematical Modeling. *AIChE J*., 56(4), 1063–1079. https://doi.org/10.1002/aic.11967.

[40] T. Numaguchi, K. Kiuchi, 1988. Intrinsic kinetics and design simulation in a complex reaction network; steam-methane reforming. *Chem. Eng. Sci.,* 43(8), 2295–2301. https://doi.org/10.1016/0009-2509(88)87118-5.

[41] W.E. Hart, J. Watson, D.L. Woodruff, 2011. Pyomo: modeling and solving mathematical programs in Python. *Math. Program. Comput.,* 3, 219–260. https://doi.org/10.1007/s12532-011-0026-8.

[42] A. Wächter, L.T. Biegler, 2006. On the implementation of an interior-point filter line-search algorithm for large-scale nonlinear programming. *Math. Program.,* 106, 25–57. https://doi.org/10.1007/s10107-004-0559-y.

[43] Department of Energy Security and Net Zero. Energy Price Guarantee (prepayment meters): regional rates and standing charges, October to December 2023. https://www.gov.uk/government/publications/energy-price-guarantee-regional-rates/energy-price-guarantee-prepayment-meters-regional-rates-and-standing-charges-october-to-december-2023 (accessed 31 October 2023).

[44] A. Finch, J. van den Bergh, 2022. Assessing the authenticity of national carbon prices: A comparison of 31 countries. Glob. Environ. Change, 74, 102525. https://doi.org/10.1016/j.gloenvcha.2022.102525.

[45] Z. Zhou, Z. Sun, L. Duan, 2023. Chemical looping: A flexible platform technology for CH_4 conversion coupled with CO_2 utilization. *Curr. Opin. Green Sustain. Chem*., 39, 100721. https://doi.org/10.1016/j.cogsc.2022.100721.

[46] P. Kotek, A. Selei, B. Takácsné Tóth, B. Felsmann, 2023. What can the EU do to address the high natural gas prices? *Energy Policy*, 173, 113312. https://doi.org/10.1016/j.enpol.2022.113312.

[47] J. David, H. Herzog, 2000. The cost of carbon capture. In *Proceedings of 5th International Conference on Greenhouse Gas Control Technologies (GHGT-5), Cairns, Australia,* 13–16. https://sequestration.mit.edu/pdf/David_and_Herzog.pdf.

[48] C. Chen, G.M. Bollas, 2020. Design and Scheduling of Semibatch Chemical-Looping Reactors. *Ind. Eng. Chem. Res*., 59(15), 6994–7005. https://doi.org/10.1021/acs.iecr.9b05693.

[49] A.d.F. Sánchez-Bautista, J.E. Santibañes-Aguilar, L.F. Fuentes-Cortés, A. Flores-Tlacuahuac, J.M. Ponce-Ortega, 2018. A Multistakeholder Approach for the Optimal Planning of Sustainable Energy Systems. ACS Sustain. Chem. Eng., 6(7), 9451–9460. https://doi.org/10.1021/acssuschemeng.8b01937.

[50] M.A. Gutiérrez-Limón, A. Flores-Tlacuahuac, I.E. Grossmann, 2014. MINLP Formulation for Simultaneous Planning, Scheduling, and Control of Short-Period Single-Unit Processing Systems. *Ind. Eng. Chem. Res*., 53(38), 14679–14694. https://doi.org/10.1021/ie402563j.

[51] M. Hossein Sahraei, L.A. Ricardez-Sandoval, 2014. Controllability and optimal scheduling of a CO_2 capture plant using model predictive control. *Int. J. Greenh. Gas Control*, 30, 58–71.

[52] S. Liu, X. Yin, J. Liu, 2023. Sensor network design for post-combustion CO_2 capture plants: Computational efficiency and robustness. *J. Process Control*, 129, 103035. https://doi.org/10.1016/j.jprocont.2023.103035.

[53] X. Yin, B. Decardi-Nelson, J. Liu, 2020. Distributed monitoring of the absorption column of a post-combustion CO_2 capture plant. *Int. J. Adapt. Control Signal Process.*, 34(6), 757–776. https://doi.org/10.1002/acs.3074.

[54] S. Liu, X. Yin, J. Liu, 2023. State estimation of a carbon capture process through POD model reduction and neural network approximation. *arXiv preprint,* 2304.05514. https://arxiv.org/abs/2304.05514.

Appendix

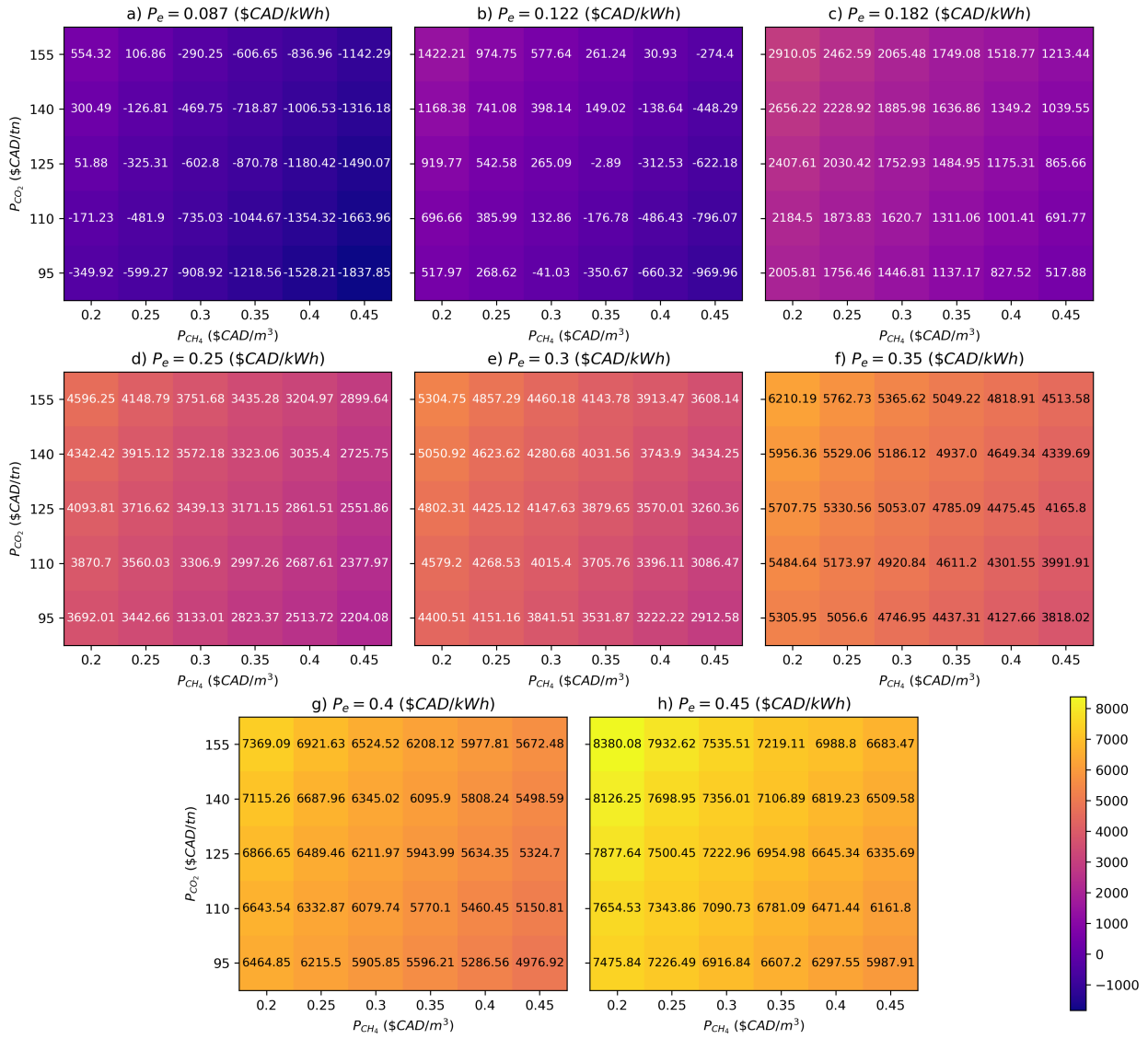

Figure A12: Joint sensitivity on overall revenue (R_{CLC}) with varying CO_2 prices (y-axes), natural gas prices (x-axes), and energy prices (subplots).

Graphical abstract